



Talik detection beneath water tracks using three-dimensional Ground-penetrating radar

Maud Henrion¹, Sophie Opfergelt¹, Maëlle Villani¹, Philippe Roux¹, Djim Verleene¹, Eléonore du Bois d'Aische^{1,2}, Maxime Thomas¹, Gilles Denis³, Edward A.G. Schuur⁴, François Jonard^{1,2}, Veerle Vanacker^{1,5}, Kristof Van Oost¹, Sébastien Lambot¹

Correspondence to: Maud Henrion (maud.henrion@uclouvain.be)

Abstract. Permafrost is degrading, raising concerns about its impact on global climate. Taliks, year-round unfrozen layers of ground in permafrost environments, affect Arctic hydrological and carbon dynamics and contribute to permafrost degradation. Despite their importance, they are seldom studied because of the difficulty in identifying them. Water tracks (zones overlying permafrost concentrating water flow) have an important role in controlling catchment hydrology, yet their contribution to talik formation remains poorly understood. The objective of this study is to detect and characterize suprapermafrost taliks in three-dimensions at high spatial resolution (dm-scale), with a specific focus on those located beneath water tracks. Fieldwork was conducted in a discontinuous permafrost area near Eight Mile Lake, Alaska (USA), during winter using a Ground-penetrating radar with a 600 MHz antenna. Ground-penetrating radar proved to be a reliable tool for imaging talik depth and extent. While talik tops were clearly detected with a root mean square error of 17 cm, their bottoms were less identifiable due to limited signal penetration. Both isolated and lateral suprapermafrost taliks were observed at the site. Importantly, taliks were more present, shallower and thicker in water tracks than in their adjacent areas. Additionally, thicker snow cover and topographic depressions were significantly associated with shallower taliks (respective significant correlations of -0.65 and 0.53). Water tracks thus appear to be hotspots for talik formation and expansion, with important implications for winter subsurface hydrological connectivity. These findings highlight the need for increased attention to the processes occurring during the winter in the water tracks environments.

1 Introduction

15

Permafrost is warming globally (Biskaborn et al., 2019), raising concerns about its potential impacts on the global climate.

Cryosols are composed of permafrost, defined as ground that remains below 0 °C for at least two consecutive years (Permafrost Subcommittee, 1988), and an active layer, the upper soil layer that freezes and thaws annually (Boike et al.,

¹Earth and Life Institute, Université catholique de Louvain, Louvain-la-Neuve, Belgium

²Earth observation and Ecosystem modelling laboratory, Université de Liège, Liège, Belgium

³Imaqa Expeditions, Brussels, Belgium

⁴Center for Ecosystem Society & Science, Northern Arizona University, Flagstaff, AZ, USA

⁵Soil Geography and Landscape Group, Wageningen University, Wageningen, the Netherlands



55



1998). Soils in permafrost regions play a key role in the global carbon cycle, as they store approximately 1460-1600 Gt of organic carbon within the upper 3 meters of soil (Burn et al., 2024). Rising Arctic temperatures are accelerating permafrost thaw, enabling the decomposition of previously frozen organic carbon and releasing greenhouse gases, mainly carbon dioxide and methane. This process may reinforce climate change through what is known as the *permafrost carbon feedback* (e.g., Koven et al., 2011; Schuur et al., 2015). Most climate models focus on greenhouse gas emissions associated with summer active layer thaw, although emissions can continue during winter, which remains understudied (Lyu et al., 2024; Natali et al., 2019).

40 These winter emissions may be linked to the presence of taliks, defined as layers of ground remaining unfrozen all year within permafrost areas (Permafrost Subcommittee, 1988). They can form close to water bodies retaining heat in winter (Lamontagne-Hallé et al., 2018), near infrastructure such as gas pipelines (Wang and Niu, 2024), or following wildfires (Rey et al., 2020). Taliks can also appear when the active layer summer thaw exceeds the winter refreezing, a process often induced by rising temperatures (Devoie et al., 2019; Schuur et al., 2008). These latest taliks are thus located between the active layer and the permafrost. The classification of taliks remains unclear, as several studies propose varying terminologies (Wang and Niu, 2024). In this study, we adopt the definition of suprapermafrost taliks, referring to taliks located above permafrost, which are classified as either 'isolated' when they are surrounded by frozen ground, or as 'lateral' when they are connected to surrounding groundwater (O'Neill et al., 2020; Permafrost Subcommittee, 1988). Recent studies indicate an increasing occurrence of taliks in the discontinuous permafrost zone (Farquharson et al., 2022), along with an expansion in their spatial distribution (Connon et al., 2018). Talik formation and expansion is favored by high soil moisture, thick snow layer, and warmer soil surface temperatures (Devoie et al., 2019).

The presence of taliks has important consequences: organic carbon within taliks continues to decompose in winter, as microbial activity persists in unfrozen conditions when water is available (Arndt et al., 2023; Devoie et al., 2024). Natali et al. (2019) report increasing carbon emissions during winter months, and Parazoo et al. (2018) estimate that taliks could emit up to 50 Pg of carbon by 2200. Additionally, laterally connected taliks enable year-round delivery of dissolved organic carbon to inland waters (Walvoord et al., 2019). Another major impact of taliks is their contribution to increased vertical permafrost thaw and the acceleration of permafrost degradation (Connon et al., 2018; Devoie et al., 2019). Despite these impacts, current permafrost models typically omit the presence of taliks, especially those associated with lateral hydrologic movement, thereby underestimating their potential influence on carbon dynamics (Arndt et al., 2023; Devoie et al., 2019; Natali et al., 2019). One of the reasons is that taliks are difficult to observe directly, making their characterization challenging (Wang and Niu, 2024). Current work on mapping the spatial extent of taliks relies on thermal, mechanical and geophysical measurements, as well as modelling (O'Neill et al., 2020). Each method has its own advantages and limitations, and a combination of approaches is often recommended (Wang and Niu, 2024). It is therefore essential to determine taliks spatial extent in order to quantify the amount of organic carbon that can potentially be degraded.



70

75

90



Water tracks are other important permafrost features, defined as unchanneled zones overlying permafrost that concentrate water flow downslope (Del Vecchio and Evans, 2025). They connect hillslopes to inland waters and act as conduits for enhanced groundwater flow (Evans et al., 2020). Compared with adjacent areas, water tracks have higher soil moisture and thicker snow cover (Del Vecchio and Evans, 2025). They may therefore be preferential sites for talik formation (Tananaev et al., 2021), but direct field evidence is currently lacking. Investigating this process is crucial because of its potential impact on catchment hydrology year-round.

Several geophysical methods are commonly used to map permafrost and identify transitions between ground layers (Walvoord and Kurylyk, 2016). Among these methods, Ground-penetrating radar (GPR) is a non-invasive technique that transmits very high to ultra-high frequency electromagnetic waves into the ground. These waves are reflected partially as they encounter a contrast in the dielectric properties of the media they propagate through (Doolittle, 1987). The reflected signals are then analyzed to image subsurface structures (Neal, 2004). Ground-penetrating radar is particularly effective for mapping thermal interfaces due to the dielectric permittivity contrasts between frozen and unfrozen layers (Moorman et al., 2003). As a result, it is widely used to determine permafrost depth (Walvoord and Kurylyk, 2016). It also enables the determination of snow thickness (Kneisel et al., 2008) and the depth of organo-mineral transition (e.g., Henrion et al., 2024). It offers several advantages, including rapid and non-destructive data acquisition. Ground-penetrating radar measurements along a transect provide two-dimensional data (position along the line and depth), while measurements on a closely spaced rectilinear grid yield three-dimensional data (mapping X and Y positions along with depth). Three-dimensional GPR surveys have attracted considerable interest (e.g., Kneisel et al., 2008), as they provide more detailed subsurface imaging. The application of GPR in permafrost environments presents several challenges. These include strong lateral variations in dielectric permittivity, difficulties in detecting steep frozen-unfrozen interfaces (> 45°), and the presence of ice lenses leading to chaotic reflections (Moorman et al., 2003). Additionally, soil cores are needed for subsurface verification, which can be challenging under winter conditions (Kneisel et al., 2008).

Given the challenges associated with characterizing taliks, GPR has been increasingly used to detect and map them. A majority of studies using GPR to detect talik has focused first on those located beneath rivers and lakes (Arcone et al., 1998b; Stevens and Moorman, 2008; You et al., 2017), as they are easier to target (Wang and Niu, 2024). Later studies have expanded to taliks found in discontinuous permafrost regions (Jones et al., 2016; Popov et al., 2025; Sjöberg et al., 2015; Yoshikawa and Hinzman, 2003). Ground-penetrating radar is particularly effective for detecting suprapermafrost taliks, as they generate strong radar reflections (O'Neill et al., 2020). Most GPR studies on taliks have applied two-dimensional imaging with frequencies ranging from 100 to 500 MHz, mostly conducted in the spring and summer months. These studies are often complemented by electrical resistivity tomography, soil cores and temperature boreholes for validation (O'Neill et al., 2020; Sjöberg et al., 2015). To our knowledge, no study has yet applied close-spaced rectilinear GPR measurements in a





grid for three-dimensional imaging of taliks. Though this approach has been widely applied in other related contexts; for instance, to map snow thickness and subsurface ice structures (Munroe et al., 2007), and active layer depth (Brosten et al., 2009; Sudakova et al., 2021). The use of grids is particularly valuable for interpreting the geometry of complex subsurface features (Moorman et al., 2003). This seem thus essential for accurately imaging taliks, which are key three-dimensional structures. Importantly, the link between water tracks and talik presence remains poorly quantified, and 3D GPR offers a promising approach to address this knowledge gap.

In this study, we present an innovative three-dimensional mapping of taliks beneath water tracks using a GPR equipped with a 600 MHz center-frequency antenna. Our survey was conducted during the winter season at Eight Mile Lake, Alaska (USA), a site representative of discontinuous permafrost conditions. By providing new insights into the structure and spatial extent of taliks, our work aims to advance the understanding of their development along water tracks. Specifically, we aim to (1) detect and map the presence of taliks, (2) determine the depth of their upper and lower boundaries, and (3) discuss the implications of their distribution along water tracks in the context of ongoing permafrost degradation.

2 Methods

110

130

2.1 Study site

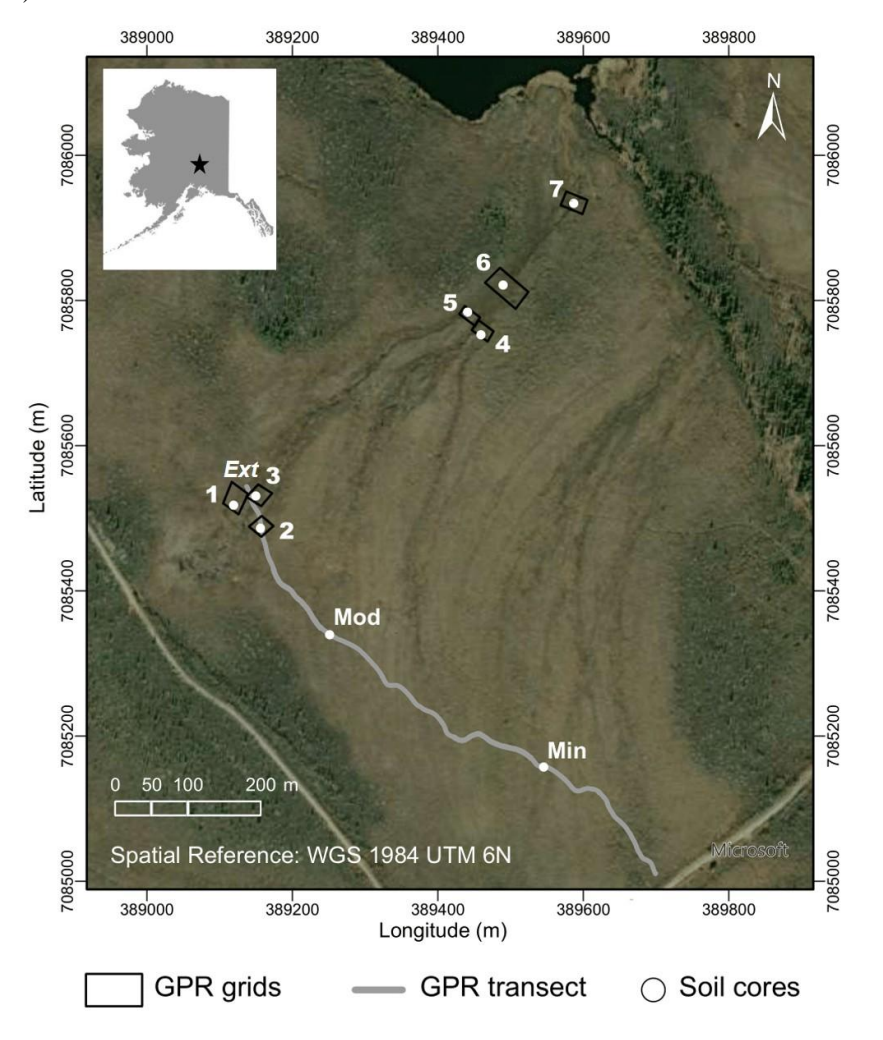
The study site, referred to as the "Permafrost Thaw Gradient" site, is located near Eight Mile Lake (63.87° N, 149.25° W), Alaska (USA), at an altitude of 700 m. The mean annual air temperature is -0.94 °C, and the average annual precipitation is 381 mm (2007-2017, National Climatic Data Center, National Oceanic and Atmospheric Administration). It is located in the discontinuous permafrost zone, with permafrost widespread at the study site. Permafrost in the area is degrading through gradual thaw, active layer deepening, ground subsidence and water table rise (Osterkamp et al., 2009; Plaza et al., 2019; Rodenhizer et al., 2020). The terrain has a gentle 4° slope. The soil is a Histic Turbic Cryosol according to the World Reference Base (WRB) system. It is composed of an organic horizon (20-55 cm thick, > 20 % carbon content) over cryoturbated mineral soil derived from glacial till and loess (Hicks Pries et al., 2012; Osterkamp et al., 2009; Vogel et al., 2009). Vegetation is dominated by the sedge *Eriophorum vaginatum*, small shrubs and *Sphagnum spp*. mosses (Mauclet et al., 2022; Schuur et al., 2007). The active layer generally ranges from 50 to 80 cm (Schuur et al., 2021) but can extend to 200 cm in subsided water tracks.

The "Gradient" site has been monitored for over 30 years to study permafrost thaw. It is characterized by variations in vegetation and active layer thickness (Osterkamp et al., 2009). A permafrost degradation gradient has been established with increasing active layer depth, ranging from minimal (Min) to moderate (Mod) and extensive (Ext) degradation (Fig. 1), evolving from little site disturbance to shallow thermokarst depressions to larger depressions, respectively (Osterkamp et al., 2009; Schuur et al., 2009). Another interest within the study site is the presence of water tracks, visible on aerial imagery





(Fig. 1). The main water track of the study site starts near the Ext position. Water tracks have expanded upslope in the watershed since 1954 (Rodenhizer et al., 2022). They are often combined with subsidence, due to the melting of permafrost ice (Del Vecchio and Evans, 2025). In this study, these features will be referred to as water tracks because, although they can exhibit steep banks and depressions ranging from 0 to 80 cm in relief, their beds are vegetated and no sediments are present along the flow path (Del Vecchio and Evans, 2025). Compared to the surrounding area, water tracks at the study site have deeper permafrost, a thicker superficial organic-rich horizon (Monhonval et al., 2023), and support dense vegetation (Rodenhizer et al., 2022).



140 Figure 1: Map of the study site near Eight Mile Lake (Alaska, USA). Ground-penetrating radar measurements were conducted along the grey transect in two dimensions, following a permafrost degradation gradient from minimal (Min), to moderate (Mod) and extensive (Ext). Three-dimensional data were collected at seven locations along a water track using grids (black squares). White dots indicate manual coring locations. Base map: Esri, Maxar, Earthstar Geographics, GIS User Community.



155

160

165



145 2.2 Field campaign conditions

The data collection was carried out from February 26th to March 5th 2024. This period corresponds to the *Deep Cold* phase, defined by Olsson et al. (2003) as a period during which the active layer has refrozen to its maximum extent. The soil temperature sensors installed at the study site (Teros12, METER Group, München, Germany) recorded an annual minimal temperature at 60 cm depth two weeks after the data collection and the minimal annual temperatures at 10 and 30 cm depth during the field campaign (Fig. 2a). The campaign was thus conducted at a period close to the annual minimum soil temperature to ensure maximum active layer refreezing and thus allowing optimal detection of any residual talik. It is worth noting that an episode of warmer air temperature appeared two weeks before the field campaign which may have caused a part of snow to melt. Air temperature (ZL6 data logger, METER Group, München, Germany) during the field campaign ranged from -33 to 0 °C (Fig. 2b).

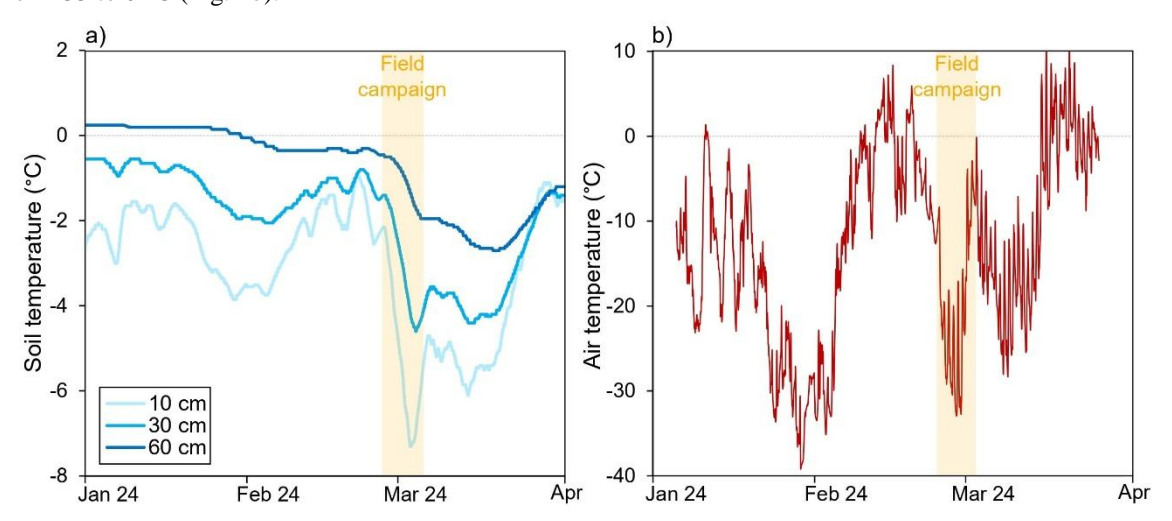


Figure 2: Evolution of soil and air temperature at the study site (Ext position) from January to April 2024. The period of the field campaign is indicated. a) Soil temperature at depths of 10, 30 and 60 cm. b) Air temperature.

2.3 Study design

Ground-penetrating radar data collection included two types of measurement extent. First, a two-dimensional GPR profile was conducted along a 900 m transect (Fig. 1) following the degradation gradient identified in previous studies (e.g., Osterkamp et al., 2009). Second, three-dimensional GPR data from seven rectilinear grids distributed along the main water track of the site were conducted (Fig. 1). In situ validation was achieved using two soil cores collected along the transect and seven cores collected along the water track. Each soil core sampling location was aligned with a vertical GPR slice for validation of the interfaces of interest detected on the GPR images (snow-frozen soil, frozen soil-top of the talik, bottom of the talik-permafrost). Both grids and soil cores have been ordered along a sequence of increasing degradation level based on permafrost depth (from shallow to deep) and position along the slope (from upslope to downslope). The least degraded cores are Min then Mod, both located on the transect and on the upslope part of the site, two areas of the intensively monitored



175

180

185

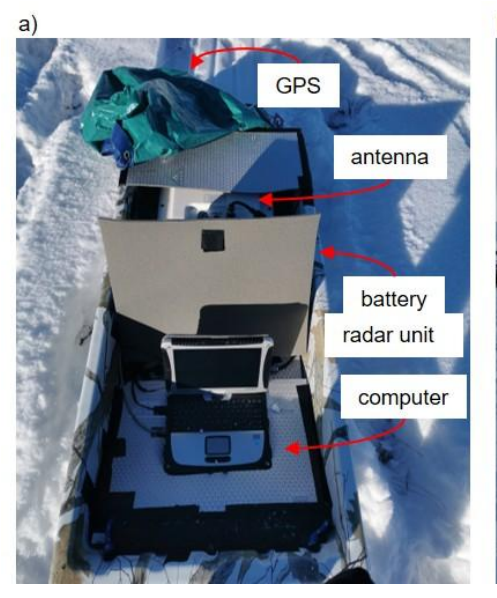


"Gradient" site. Grids are then arranged in order of position along the slope as follows: Grid 1, Grid 2 and Grid 3 in the upslope area; Grid 4, Grid 5 and Grid 6 in the middle slope area; Grid 7 in the downslope area. Grids 1 and 2 are situated near the initiation zones of water tracks, in areas with scattered surface subsidence, whereas Grids 3 to 7 are located distinctly on water tracks.

2.4 Ground-penetrating radar measurements

2.4.1 Ground-penetrating radar survey setup

In this study, we used a RIS MF Hi-Mod GPR (IDS Georadar, Pisa, Italy) equipped with a 600 MHz center-frequency antenna. The positions of radar measurements were recorded using an EMLID Reach RS+ differential GPS (EMLID, Budapest, Hungary) at a frequency of 1 second. The radar was mounted on a sledge (Fig. 3a). Given the low air temperatures encountered (Fig. 2b), the main radar components were insulated using foam. The GPR measurements were acquired at a rate of 72 traces per second. The sledge was pulled manually at a speed of approximately 1.5 to 2 km h⁻¹ (Fig. 3b), resulting in GPR measurements spaced roughly every 7 mm. First, GPR measurements were acquired in two dimensions along the transect. Then, three-dimensional measurements were acquired in grids at seven locations along the water track. Grid areas ranged from 350 to 1515 m², with line spacing between 1 and 2 m (precise dimensions of the grids provided in Table A. 1. Data processing is composed of five main steps described below: (1) cleaning the GPS data, (2) post-processing each 2D GPR image, (3) selecting the interfaces of interest on each 2D image, (4) combining the 2D images of the grids to generate 3D data, and (5) estimating the relative dielectric permittivities (ϵ_r) of snow, frozen active layer and taliks to determine the depths of the selected interfaces. The data processing was performed using the Geolitix software (Geolitix Technologies Inc., Vancouver, Canada).







190

195

200

205

210



Figure 3: Ground-penetrating radar device configuration and measurements. (a) The sledge contains the GPR device, composed of the radar connected to the antenna, a battery and a computer. An external GPS is also mounted on the sledge. Insulation was applied around the key components to protect them from the cold, and a cap was placed on the sledge during measurements. (b) Measurement procedure on a grid.

2.4.2 Ground-penetrating radar data processing

First, GPS data were filtered to exclude low-accuracy positions, with a maximum Horizontal Dilution of Precision (HDOP) of 2 and a minimum of 6 satellites. The locations were then smoothed using a moving average window of 10. Finally, the terminal sections, where the GPR turned at the grid limits, were removed from the dataset.

Second, the GPR images were visualized with two-way travel time on the vertical axis, representing depth in time, and linear distance on the horizontal axis, after resampling traces to be equidistant every 1 cm. The following processing steps were applied to the GPR data to optimize image visualization (Daniels, 2004): (1) time-zero correction, to remove the signal before the soil surface, using the "find positive peak" method; (2) band-pass frequency filtering from 120 to 1500 MHz, to reduce noise in the data; (3) dewow filtering, to remove low frequency noise; (4) background subtraction, to remove horizontal artifacts caused by antenna ringing; (5) gain adjustment, to enhance contrast at greater depths, using the "energy decay" method based on the mean amplitude decay curve; (6) constant gain of 16 dB, to amplify contrasts; (7) time cut at 30 ns, as deeper data were too noisy. To facilitate the identification of specific interfaces, a Sobel transform, an edge detection method that computes the gradient of the image intensity (Daniels, 2004), was temporarily applied for visual inspection.

Third, the interfaces of interest were identified and selected. These interfaces include: snow – frozen soil surface, frozen soil – talik top, talik bottom – permafrost. These interfaces are expected to appear in the GPR images as zones of strong reflection, due to the high electromagnetic contrast between the horizons. They were manually selected when clearly identifiable using the "horizon interpretation" tool. While Geolitix provides an algorithm for automatic horizon delineation, it introduces small-scale noise in the depth data and was therefore not used. Nevertheless, our manual picking was compared with the algorithm's results to ensure consistent overall patterns.

Fourth, the depth of the interfaces of interest was mapped continuously in the grids using the "depth grid" and the "thickness grid" features. This was achieved based on the interfaces selected in each GPR image and kriged with a cell size of 10 cm, a search radius of 2.5 meters, and a moving average with a window width of 3 cells. When an interface, such as the talik top, was not continuous, the interpolation was cut with a diameter of 1.25 m around the identified features. This allowed the creation of snow thickness maps, as well as maps of the depth of the top of the taliks. For talik detection, the percentage of the grid area where taliks were found was then calculated. Horizontal planar slices were also extracted from the three-dimensional GPR data. This helps identify areas with uniform amplitudes and contrasts in the subsurface across the area of interest. The slices were generated after applying a Hilbert transform to the data, which removes the negative component of



225

230

235

240

245



the GPR traces (Daniels, 2004). These horizontal slices are presented in this study at the depths corresponding to the upper part of the taliks when present, to highlight their position and the heterogeneity of the subsoil. Zones of high amplitude on these horizontal slices represent generally areas of higher soil moisture.

2.4.3 Determination of the relative dielectric permittivities of the subsurface layers

The relative dielectric permittivities (ε_r) of the subsurface layers identified on the GPR images were estimated to enable the estimation of their depths. The ϵ_r indeed controls the wave propagation speed, and enable to convert time taken by the waves to reach an interface to depth. To estimate the ε_{r} of the different layers, different methods were used and compared: (1) literature values, (2) on-site measurements using Teros12 sensors placed at three positions in the study site, with depths ranging from 0 to 60 cm, and (3) theoretical hyperbola fitting in Geolitix (e.g., Ardekani et al., 2014). A summary of the results from these methods is presented in Table 1. The first layer of interest is snow. Snow density measurements on-site yielded an approximate density of 0.26 g/cm^3 . According to previous studies, this corresponds to a ε_r ranging from 1.4 to 1.5 (Di Paolo et al., 2018; Evans, 1965; Hallikainen et al., 1986). The ε_r estimation based on the hyperbola forms gives a mean of 1.5. Therefore, a ε_{Γ} of 1.5 was chosen for snow, as it aligns with both methods. The second layer of interest is frozen soil. Literature values for ε_r range from 3 to 9, with most values around 5 - 5.5 (Arcone et al., 1998b; He and Dyck, 2013; Hinkel et al., 2001; Kneisel et al., 2008; Moorman et al., 2003; Munroe et al., 2007; Ortet et al., 2025; Watanabe and Wake, 2009). The Teros12 sensors measured a ε_r of 5. The mean ε_r based on the hyperbola method was 5.4. As a result, a ε_r of 5 was chosen for frozen soil, aligning well with these three methods. The third layer of interest is unfrozen soil, corresponding to taliks. The ε_r of taliks can vary greatly depending on their water content (with higher humidity leading to higher ε_r) and is expected to exhibit more variability than frozen soil. Literature values for ε_r are 17 (Pan et al., 2014), 25 (Kneisel et al., 2008), 30 (Arcone et al., 1998b), and 50 (Moorman et al., 2003), depending on the actual soil moisture. The hyperbola method on upslope grids (Grids 1, 2, 3) gave a mean ε_r of 11, while the mean for the middle slope grids (Grids 4, 5, 6) was 26. This method was not feasible on Grid 7 (downslope), but note that water ponding was visible there, indicative of waterlogged conditions. Generally, a moisture gradient was observed in the taliks as one moved down the water track. Based on these observations, the ε_r for the taliks was estimated as follows: 15 upslope (Grids 1, 2, 3), 25 for the middle slope (Grids 4, 5,6), and 40 downslope (Grid 7). These values correspond to volumetric water contents of 0.28, 0.40, and 0.51, respectively, following Topp and Davis (1985) calibration for mineral soils, or of 0.35, 0.51, and 0.70 using the Pepin et al. (1992) calibration for peat soils.





250 Table 1: Estimation of the er of the different subsurface layers based on literature, Teros12 sensors, manual hyperbola detection and final choice for this study.

	Relative dielectric permittivity (dimensionless)					
Layer	Literature	Teros12	Hyperbolas (mean ±	Final choice for		
			sd)	this study		
Snow	1.4 - 1.5	NA	$1.5 \pm 0.5 (n=19)$	1.5		
Frozen soil	3 to 9 (mainly 5 -	5	$4.7 \pm 3.3 \ (n=56)$	5		
	5.5)					
Taliks upslope (Transect,			$11 \pm 9 \ (n=14)$	15		
Grids 1, 2, 3)						
Taliks middle slope (Grids	17 to 50	NA	$26 \pm 16 \ (n=24)$	25		
4, 5, 6)						
Taliks downslope (Grid 7)			NA	40		

2.5 Soil coring

Nine soil cores were collected using a gas-powered auger along the transect and the water track (Fig. 1). The position of these cores was recorded using a non-differential GPS (inReach Mini 2, Garmin Ltd., Olathe, USA) with a 5 m resolution.

For each soil core, the snow depth was measured. The depth of the top and the bottom of the talik, when present, was recorded. For the transect of interest, the snow depth was also measured every 20 m. Knowing the depth of the transition between organic and mineral layers in the subsoil is important when interpreting GPR images, as this interface can also generate wave reflections (Henrion et al., 2024). However, it was not clearly identifiable on the collected soil cores.

2.6 Local topographic site data

For each GPR grid, the topographic position index (TPI) was used to indicate whether a location lies on a flat area, a ridge, or a valley by comparing its elevation to the mean elevation of the surrounding area (Weiss, 2001). The TPI at each point was calculated based on its elevation relative to the surrounding 25 m, with a 20 cm resolution. A positive TPI indicates a ridge and a negative one a valley. The same color scale was used across the entire study site to allow comparison of the amplitude of subsided areas.

265 3 Results

270

3.1 Soil cores description

The different layers observed in the soil cores were snow, frozen active layer, talik (when present), and permafrost (Fig. 4). A clear pattern appears in permafrost depth along the degradation sequence (defined in Sect. 2.3): it is shallowest at Min (50 cm), intermediate at Mod, core 1, and core 2 (85-90 cm), and reaches greater depths in cores 3 and 4 (130 and 104 cm, respectively). In cores 5, 6, and 7, permafrost was not reached with the probes and was below 100, 112, and 180 cm, respectively. Snow depth also reflects site degradation. It remains low (< 30 cm) in areas non-affected by subsidence,



280



namely Min, Mod, and cores 1 and 2. In contrast, it is higher (> 50 cm) in subsided zones (cores 3 to 7). Regarding the presence of taliks, they were only observed on cores collected along the water track. Their upper boundary is progressively shallower along the degradation sequence, from a maximum depth of 67 cm in core 1 to a minimum one of 13 cm in core 7 (Fig. 4). Core 5 is an exception because it was located on the border rather than in the center of the water track. The talik thickness is also increasing along the sequence, with a minimal one in core 1 (18 cm) and a maximum one in core 7 (> 165 cm). It is worth noting that the observed humidity of these taliks is also increasing while going downslope. To summarize, the degradation sequence presented is characterized by increasing snow thickness, decreasing depth to the top of talik, and increasing talik thickness, from the least to the most degraded zone.

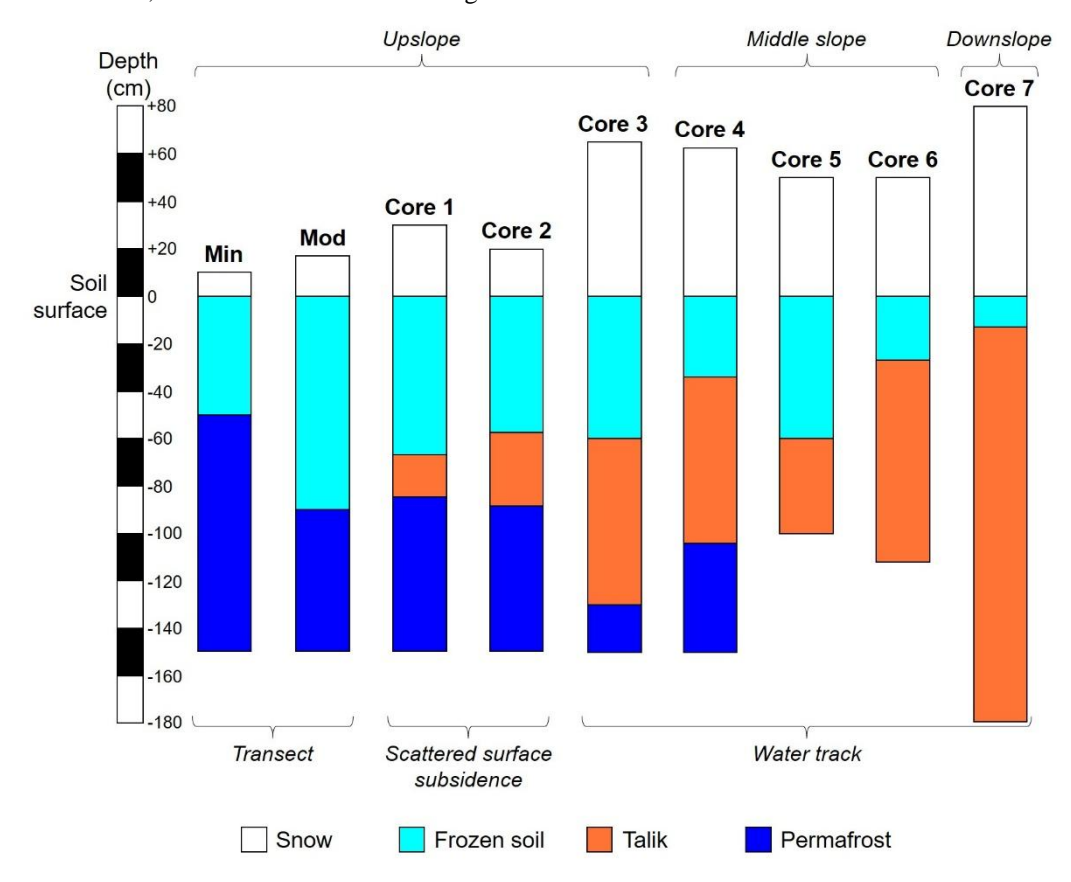


Figure 4: Stratigraphic profiles of the soil cores collected around the study site, arranged from left to right following the defined degradation sequence. The different layers identified are shown: snow, frozen soil, talik (if present), and permafrost. Where the permafrost depth is not indicated, it extends below the bottom of the core.



290



285 3.2 Ground-penetrating radar transect

Two dimensional GPR data were first acquired along a transect following a degradation gradient (Fig. 1). The snow depth along the transect ranged from 7 to 74 cm, with a mean of 31 ± 12 cm. Taliks were identified along certain segments of the transect, more specifically on 35 % of the transect between the Ext and Mod positions and on 10 % between Mod and Min. The depths to the top of these taliks ranged from 18 to 102 cm with a mean of 51 ± 14 cm. Where the upper interface of taliks was detected, the lower boundary could also be identified over 18 % of these segments, allowing for an estimation of talik thickness. However, this estimation should be interpreted with caution as it depends strongly on the ϵ_r of the talik, which was only approximated (here at 15) and varies spatially. The estimated talik thickness ranged from 7 to 57 cm, with a mean of 29 ± 13 cm.

Figure 5 presents three 70 m long GPR sections realized near the Ext, Mod, and Min sites of the "Gradient". At the Ext site (Fig. 5a), upper talik interfaces were identified at three locations corresponding to subsided areas. Taliks tops lie at depth between 19 and 87 cm, and their thickness ranged from 17 to 56 cm. The taliks in this area appear to be isolated and restricted to local subsidence zones. At the Mod site, no talik was observed on the soil core. However, the GPR image suggests the close presence of a talik (Fig. 5b) at depths between 24 and 48 cm, in a zone associated with surface subsidence.

Taliks in this zone seem more sporadic and confined to isolated depressions and are less frequent than at the Ext site. At the Min site, no talik was detected (Fig. 5c), which is consistent with the soil core. However, some interfaces of higher reflectivity were observed, which may correspond to the upper permafrost boundary if it has different electromagnetic properties than the frozen active layer. While no talik appears to be present in this area, it is noteworthy that the soil structure seems highly heterogeneous, with multiple localized reflection hyperbolas, possibly linked with ice content.





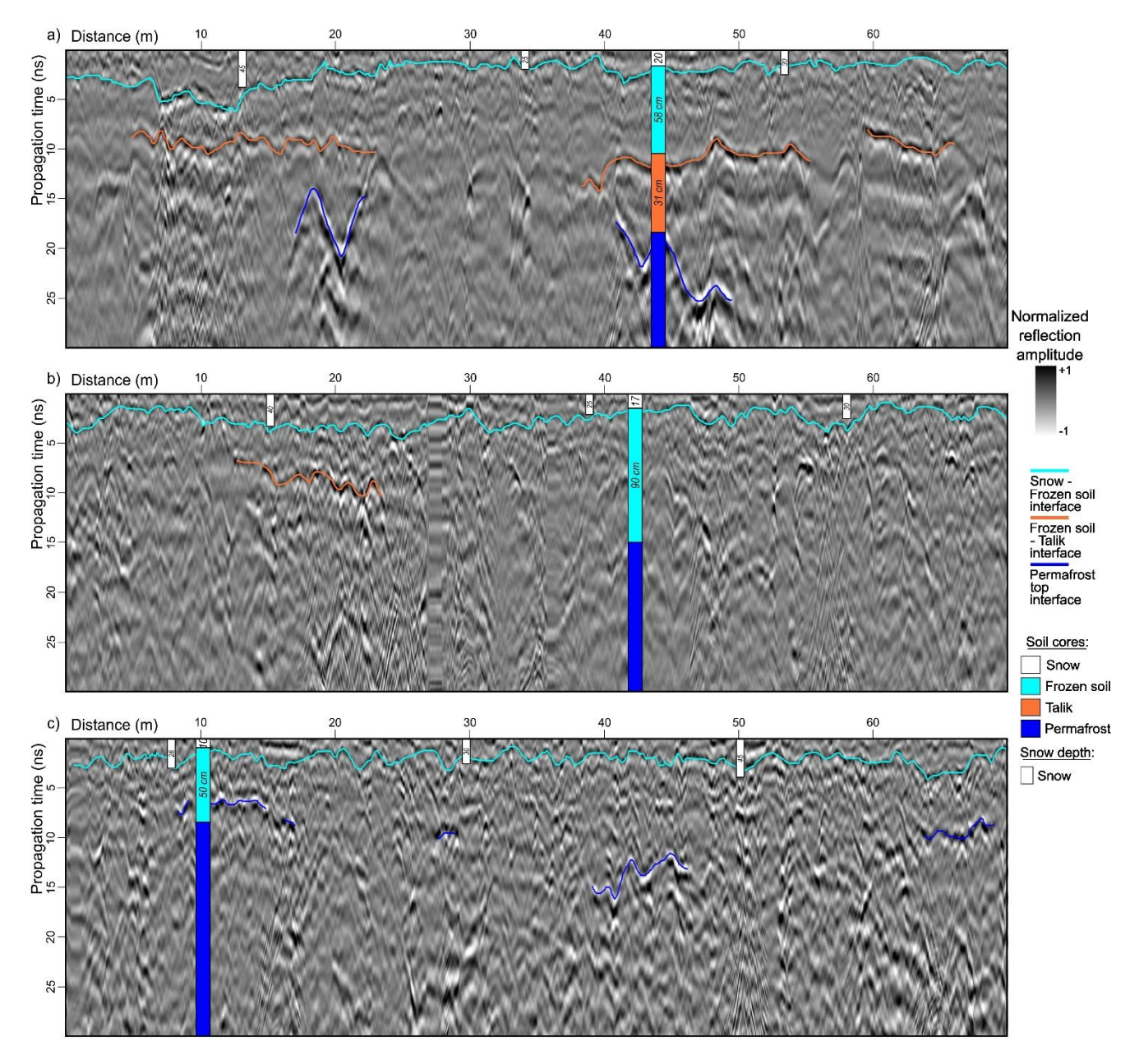


Figure 5: Three vertical 70 m long GPR slices from the transect crossing the "Gradient" site, with the interfaces of interest displayed. a) Slice in the Ext zone, the presented soil core is core 2. b) Slice in the Mod zone, the presented soil core is core Mod. c) Slice in the Min zone, the presented soil core is core Min.



315



310 3.3 Upslope GPR grids

Grids 1 and 2 are located in a mostly flat area exhibiting small, localized subsidence features (Fig. B.1a, Fig. 6a), whereas Grid 3 lies at the onset of a water track (Fig. B.2a). The horizontal GPR slices from Grids 1 and 2 reveal discrete zones of higher reflection that do not clearly correspond to the subsided areas but suggest a heterogeneous subsurface (Fig. B.1b, Fig. 6b). In contrast, in Grid 3, the areas of higher reflection approximately follow the water track path, potentially indicating higher water content (Fig. B.2b). Snow thickness in the upslope area ranges from 3 to 98 cm, with mean values of 25 cm for Grids 1 and 2, and 41 cm for Grid 3 (Table 2). Thicker snow is observed in subsided areas (Fig. B.1c, Fig. 6c) and in the water track (Fig. B.2c).

Taliks were detected across 50 %, 90 % and 75 % of the grids area in Grids 1, 2, and 3, respectively (Table 2). Talik tops were identified at depths ranging from 19 to 89 cm, being slightly shallower in Grid 3 (mean of 50 cm) compared to Grids 1 and 2 (means of 56 and 55 cm, respectively, Table 2). These depths are close to the mean ones found on the transect, also located on the upslope part of the site. Taliks appear shallower in areas with greater subsidence and thicker snow cover and are particularly shallow (< 40 cm) along the water track path in Grid 3 (Fig. B.1d, Fig. 6d, Fig. B.2d). Talik bottoms were identified in portions of Grids 1 and 2, covering respectively 70 % and 50 % of the area where talik tops were detected.

Estimated talik thickness ranges from 7 to 68 cm in Grids 1 and 2, with respective mean values of 26 cm and 33 cm (Table 2), close to the mean thickness of taliks detected on the transect. Talik bottoms were not identified in Grid 3, but taliks are expected to be thicker there, especially along the water track (70 cm thick talik at the soil core location).

The soil core in Grid 2 aligns well with the three interfaces identified with the GPR: snow-frozen soil interface, frozen soiltop of the talik interface, and bottom of the talik-permafrost interface (Fig. 6e). In Grid 3, a slight discrepancy appears
between the identified frozen soil-talik interface on the GPR slice and the soil core data (Fig. B. 2e), suggesting a positioning
error or an overestimation of the talik top depth identified with the GPR in the water track.





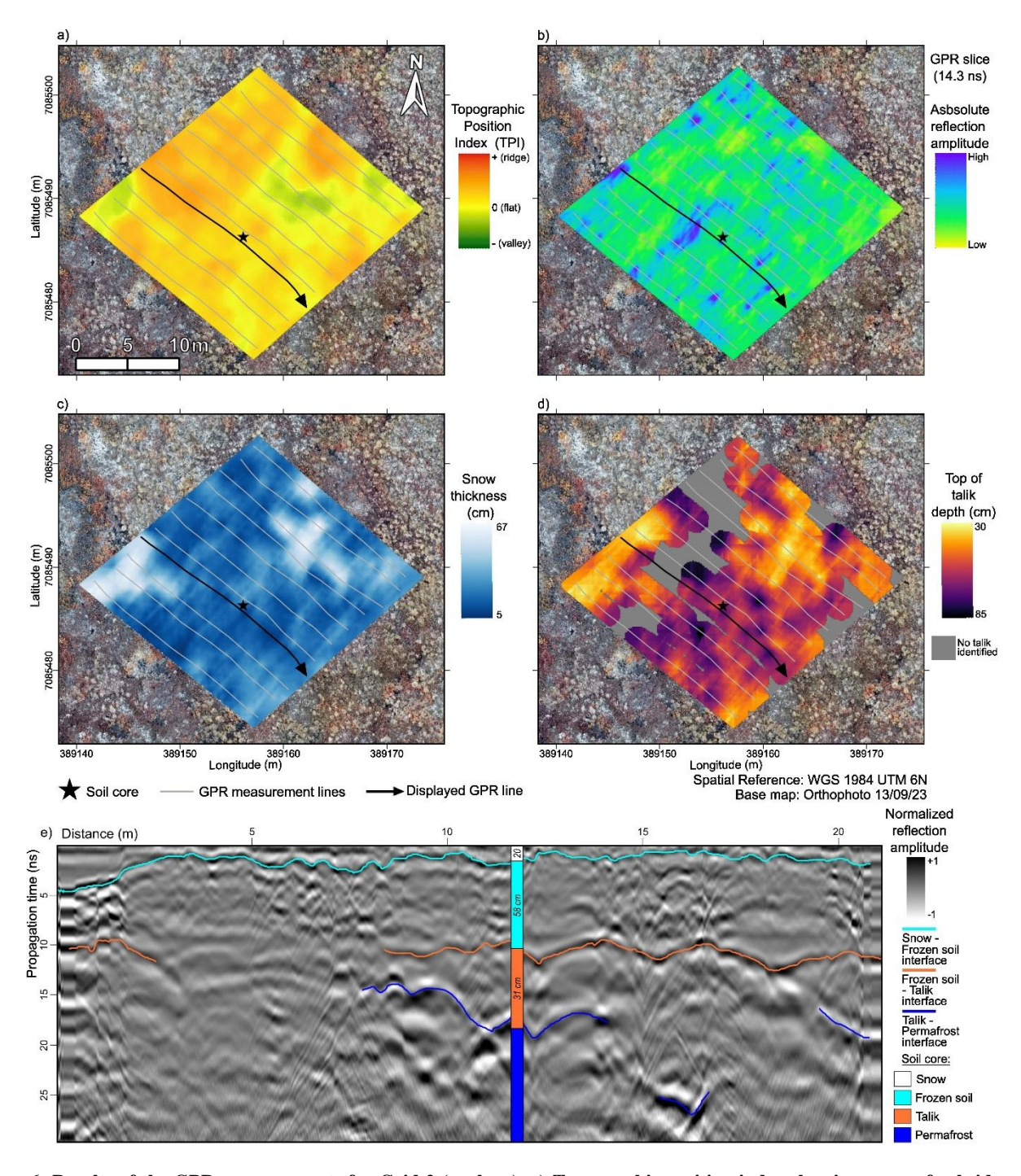


Figure 6: Results of the GPR measurements for Grid 2 (upslope). a) Topographic position index showing areas of subsidence. b) GPR horizontal slice at 14.3 ns two-way travel time, highlighting zones of strong reflections. c) Snow thickness derived from the GPR data. d) Depth of the top of the talik as interpreted from the GPR images. The grey area indicates locations where no talik was present or where it could not be identified with sufficient certainty. e) Vertical GPR slice at the soil core location, with visible interfaces of interest.





Table 2: Main variables derived from soil cores and GPR measurements (snow thickness, top of talik depth, talik thickness and permafrost depth). The percentage of each grid area where taliks were detected is also presented, as well as the percentage of the grid area with an identified talik top where the talik bottom was also detected. For GPR-derived measurements, the range of values encountered in the grids is presented along with the grid mean, following this format: min – max (mean). A precise comparison between the depths of the horizons of interest in the grids and on the GPR images is provided in Fig. 9.

		Upslope				Downslope		
Variable	Method	Grid 1	Grid 2	Grid 3	Grid 4	Grid 5	Grid 6	Grid 7
Snow thickness (cm)	GPR	5 – 63	5 – 67	3 – 98	19 – 112	11 - 111	9 – 125	12 – 119
		(25)	(25)	(41)	(61)	(44)	(51)	(56)
	Soil core	30	20	65	63	50	50	80
% of grid area where talik is detected	GPR	50 %	90 %	75 %	90 %	75 %	60 %	85 %
Top of talik depth (cm)	GPR	25 - 85 (56)	30 - 85 (55)	19 – 89 (50)	20 - 70 (42)	19 – 83 (43)	13 - 76 (33)	11 – 87 (45)
	Soil core	67	58	60	34	60	27	13
% of area with talik top detected where talik bottom is identified	GPR	70 %	50 %	0 %	0 %	30 %	0 %	0 %
Talik thickness (cm)	GPR	10 – 53 (26)	7 – 68 (33)			15 – 58 (38)		
	Soil core	18	31	70	70	> 40	> 85	> 167
Permafrost depth (cm)	Soil core	85	89	130	104	> 100	> 112	> 180

345 3.4 Middle slope GPR grids

350

355

Grids 4 and 5 are both located in places where water track arms converge. Grid 4 includes a well-defined water track arm in the west and an area of ongoing degradation in the east (Fig. B. 3a), while Grid 5 is composed of two distinct water track arms separated by a ridge (Fig. 7a). Grid 6 is located directly downslope from Grids 4 and 5, just below the convergence of three water track arms (Fig. B. 4a). As a result, the water track is wider there, and the grid size was increased accordingly. Horizontal GPR slices show partial correspondence with the water track paths: some areas of high reflection amplitude are located within these water tracks, suggesting increased water content, although this association is not systematic (Fig. B. 3b, Fig. 7b, Fig. B. 4b). Snow thickness is higher than in the upslope area and ranges from 9 to 125 cm, with mean values of 61, 44, and 51 cm for Grids 4, 5, and 6, respectively (Table 2). In all three grids, snow thickness shows a good agreement with the subsided areas of the water tracks (Fig. B. 3c, Fig. 7c, Fig. B. 4c).

Regarding talik presence, an interface corresponding to talik tops was identified almost everywhere (> 90 % of the area) in Grid 4 (Fig. B. 3d). In Grid 5, taliks were identified in both water track arms (covering approximately 75 % of the grid area), but were absent on the elevated ridge separating them (Fig. 7d). In Grid 6, talik identification was limited to 60 % of the total



360

365

375

380



grid surface (Fig. B. 4d), largely because almost no taliks were detected outside the water track. Nevertheless, their presence in these areas is likely, with the absence of detection probably resulting from a masking effect caused by strong GPR reflections within the water track. Talik tops were found at depths ranging from 13 to 83 cm in the middle slope area, with the shallowest values in Grid 6 (mean of 33 cm) compared to Grid 4 and 5 (mean of 42 and 43 cm, Table 2). In Grid 4, no clear spatial pattern appears in the talik depth except for a zone with deeper taliks along the eastern edge of the western water track (Fig. B. 3d). The zone of Grid 4 seems quite heterogeneous and in ongoing degradation. In Grids 5 and 6, talik depths align with the water tracks, with taliks generally shallower than 40 cm in Grid 6 and 50 cm in Grid 5 in the water tracks (Fig. 7d, Fig. B. 4d). In the middle slope area, talik bottoms were only identified in Grid 5 (in 30 % of the areas where their top was detected). Taliks were 15 to 58 cm thick (mean of 38 cm, Table 2) and were thinner (< 40 cm) near the water track edges than in their central zone. In Grid 6, the soil core showed a thick talik of at least 85 cm. Soil cores across the middle slope area show good correspondence with the GPR interpretations (Fig. B. 3e, Fig. 7e, Fig. B. 4e).

370 **3.5 Downslope GPR grids**

Grid 7 was conducted near the end of the water track (Fig. 8a), approximately 175 m from the lake. In this area, permafrost degradation is more advanced, and the water track appears to be transitioning into a thermokarst gully, as surface sediments were observed during summer (Del Vecchio and Evans, 2025). The horizontal GPR slice reveals a clear pattern, with a zone of high reflection amplitude in the center of the water track (Fig. 8b). This may indicate higher water content, which was confirmed by the presence of gravitational water during soil coring. Snow thickness ranges from 12 to 119 cm, with a mean of 56 cm (Table 2) and follows topographic patterns closely (Fig. 8c). Taliks were detected across approximately 85 % of the grid, though their identification was more difficult outside the water track due to weaker GPR signal contrasts, similarly as for Grid 6 (Fig. 8e). Although taliks were difficult to detect outside the water track, they likely extend across the entire grid, considering the deep permafrost detected at the soil core (> 180 cm). The depth of talik tops ranged from 11 to 87 cm, with a mean of 45 cm (Table 2). Both snow thickness and talik depth fall within the same range as observed in the middle slope area (Table 2). Similarly, as in the middle slope, talik tops within the water track were systematically shallower than 40 cm (Fig. 8d). Talik bottoms could not be identified due to their important thickness (> 167 cm at the soil core). There is a good correspondence between the soil core and the GPR image (Fig. 8e).





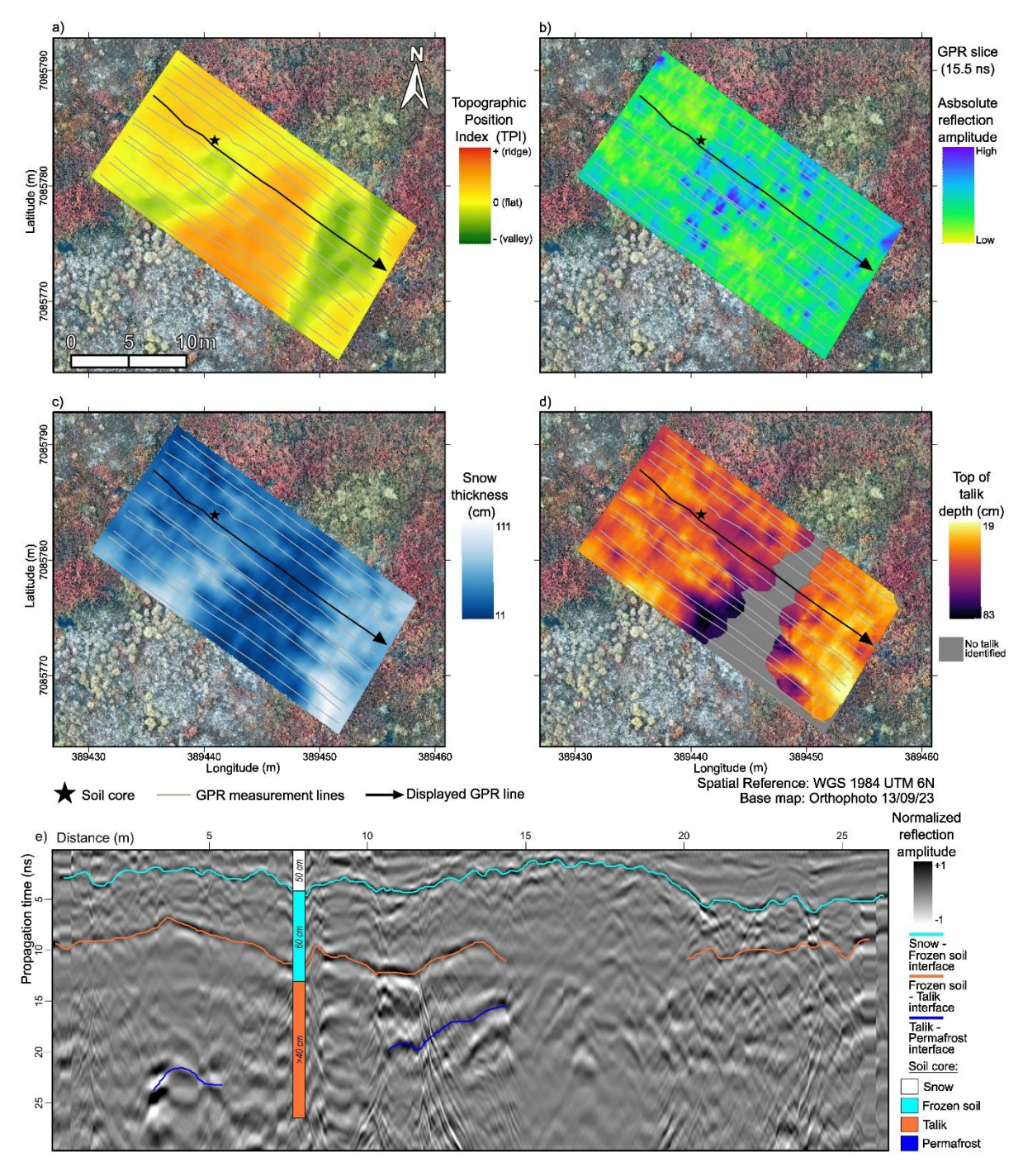


Figure 7: Results of the GPR measurements for Grid 5 (middle slope). a) Topographic position index showing areas of subsidence. b) GPR horizontal slice at 15.5 ns two-way travel time, highlighting zones of strong reflections. c) Snow thickness derived from the GPR data. d) Depth of the top of the talik as interpreted from the GPR images. The grey area indicates locations where no talik was present or where it could not be identified with sufficient certainty. e) Vertical GPR slice at the soil core location, with visible interfaces of interest.





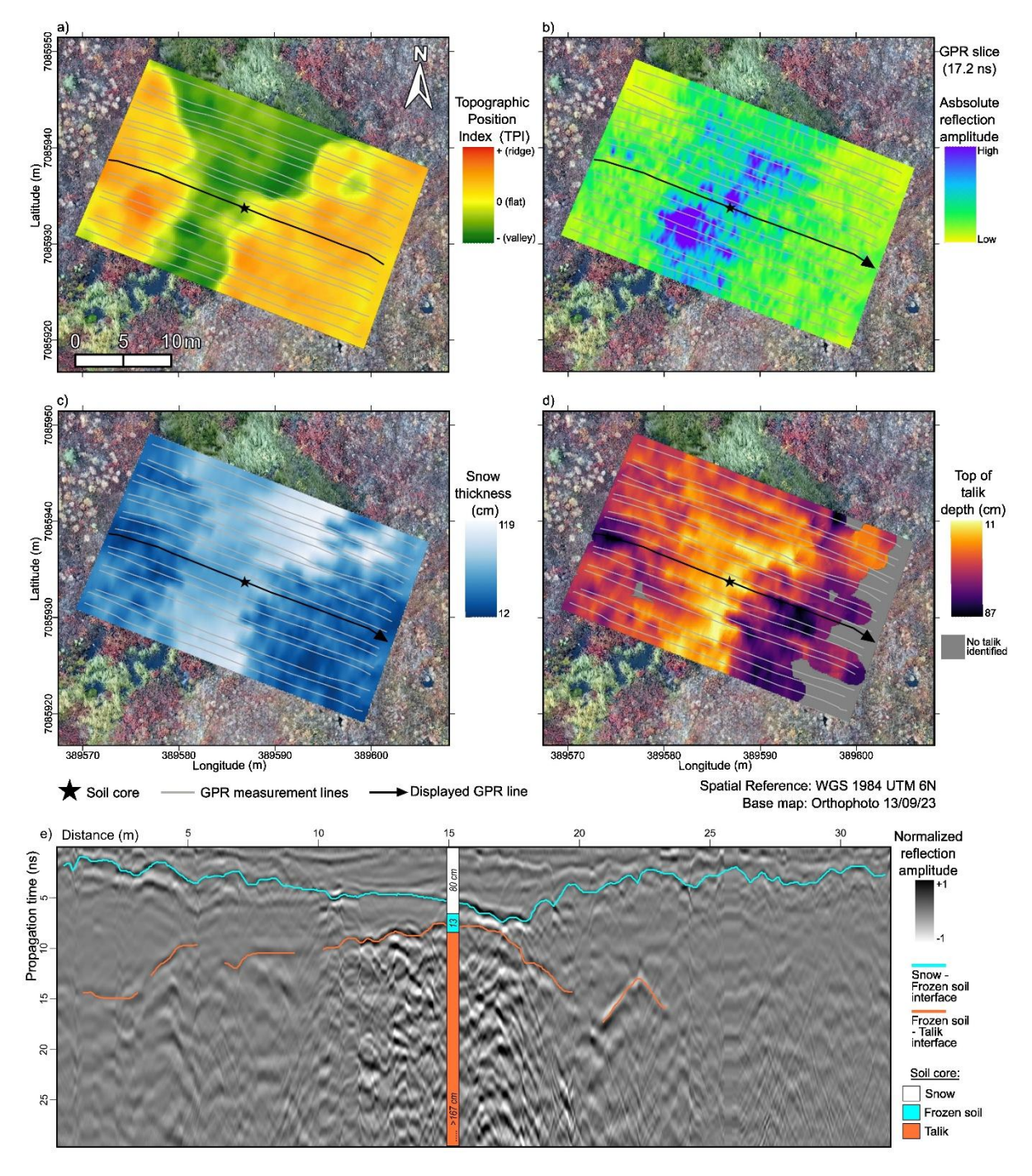


Figure 8: Results of the GPR measurements for Grid 7 (downslope). a) Topographic position index showing areas of subsidence. b) GPR horizontal slice at 17.2 ns two-way travel time, highlighting zones of strong reflections. c) Snow thickness derived from the GPR data. d) Depth of the top of the talik as interpreted from the GPR images. The grey area indicates locations where no talik was present or where it could not be identified with sufficient certainty. e) Vertical GPR slice at the soil core location, with visible interfaces of interest.





4 Discussion

4.1 Interfaces identified with the GPR and precision of the method

The first interface identified in the GPR images was the snow – frozen ground boundary, corresponding to the soil surface, which allowed for the determination of snow depth variations. Ground-penetrating radar is well established for mapping snow thickness (Kneisel et al., 2008). In this study, snow depth was characterized with a Root Mean Square Error (RMSE) of 8 cm (n = 9 soil cores, Fig. 9). Additionally, the 3D kriging of snow depth showed good consistency between adjacent lines and coherent behavior with local topography. Given this accuracy, the chosen ε_r of 1.5 for snow appears accurate. Some imprecision may occur in shallow areas (observed by Hinkel et al., 2001 for snow cover < 20 cm) or where dense vegetation trapped in the snow causes chaotic reflections.

405

410

415

400

The second interface identified corresponded to the tops of taliks. This interface is expected to produce strong reflections on GPR images due to the high contrast in dielectric properties between frozen and unfrozen soil (Moorman et al., 2003). Taliks have previously been observed with GPR in lakes, ponds, and delta environments (Arcone et al., 1998b; Stevens and Moorman, 2008; Yoshikawa and Hinzman, 2003) as well as for supra-permafrost taliks (Jones et al., 2016; Sjöberg et al., 2015; Sudakova et al., 2021). In this study, the talik tops were identified with an RMSE of 17 cm (n = 6), with some overand underestimation (Fig. 9), suggesting the ε_r value of 4.5 for frozen soil is appropriate. Accuracy was generally good, except for core 3, where a 40 cm discrepancy was observed between the core and GPR-derived talik top (Fig. B. 2e). This may be due to GPS positioning errors for the soil core (up to 5 m). This interface was detected in a high proportion of the GPR data, although some taliks likely remained undetected. Taliks tops were more easily identified within water tracks, where the higher talik moisture content generates stronger reflections. These reflections dominate the GPR signal, making the weaker reflections outside the water tracks less visible. Additionally, high signal attenuation in frozen silts and clays may further limit GPR interpretation (Arcone et al., 1998a; Davis et al., 1976). Talik detection was more reliable in grids than in the transect, as lateral coherence between adjacent lines helps interpretation (Moorman et al., 2003).

1

425

420

been imaged using GPR studies of suprapermafrost taliks by Jones et al. (2016), Sjöberg et al. (2015) and Sudakova et al. (2021). In this study, it was clearly identified at only one core location (core 2), with a 4 cm difference between GPR and core observation. Overall, this interface was not very visible, it was only detected in parts of Grids 1, 2, and 5. This is due to the fact that the antenna only allowed visibility down to 30 ns (two-way travel time), which was insufficient to reach the bottom of thick taliks. In addition, radar penetration depth decreases with increasing moisture content (typical of taliks), and the signal is further attenuated in thawed fine-textured sediment (Arcone and Delaney, 1982; Hinkel et al., 2001). Consequently, signal penetration may sometimes be restricted to the first frozen-unfrozen interface (Stevens and Moorman, 2008). Another difficulty arises from the possibility of a gradual transition at the talik bottom in terms of temperature and

The third interface of interest was the bottom of the talik, corresponding to the permafrost top. This interface has previously





moisture, which causes a misinterpretation of the permafrost table (Stevens and Moorman, 2008). Even when the talik bottom was identified, its depth should be interpreted with caution, as it strongly depends on the estimated ε_r of the talik, which was only broadly estimated and may vary strongly laterally. Finally, the lateral edges of taliks were generally not visible in this study, except for some traces in Grid 5 (Fig. 7e). This may be due to steeply dipping thermal interfaces along topographic breaks, which are poorly detected by GPR (principally when it exceeds 45°, Moorman et al., 2003).

Some other subsurface interfaces of interest were not identified in this study. First, the identification of the permafrost top in areas without taliks (thus the interface between the frozen active layer and the permafrost) should be possible when permafrost has a higher ice content (Hinkel et al., 2001). In this study, it seemed visible in parts of the transect near the Min area (Fig. 5c), though with limited confidence. This interface is known to be difficult to detect due to cryoturbation in permafrost environments (Hinkel et al., 2001). Second, in this study, the interface between the organic and the mineral soil layer was not identified. Sjöberg et al. (2015) were able to image it in unfrozen areas, while Hinkel et al. (2001) could not when it was too shallow. In this study, the organo-mineral transition likely lies in the frozen soil part for upslope grids, making it undetectable. The transition might be present in the taliks for the other grids, but it was still not detected, probably due to a nearly water-saturated mineral layer, which reduces contrast with the organic layer. Additionally, there is not a very clear boundary between the organic and the mineral soil layers at this site, because of cryoturbation (Hicks Pries et al., 2012). Although not feasible in this study, detecting the organo-mineral interface remains of interest because peat thickness influences active layer dynamics and talik formation (Atchley et al., 2016).

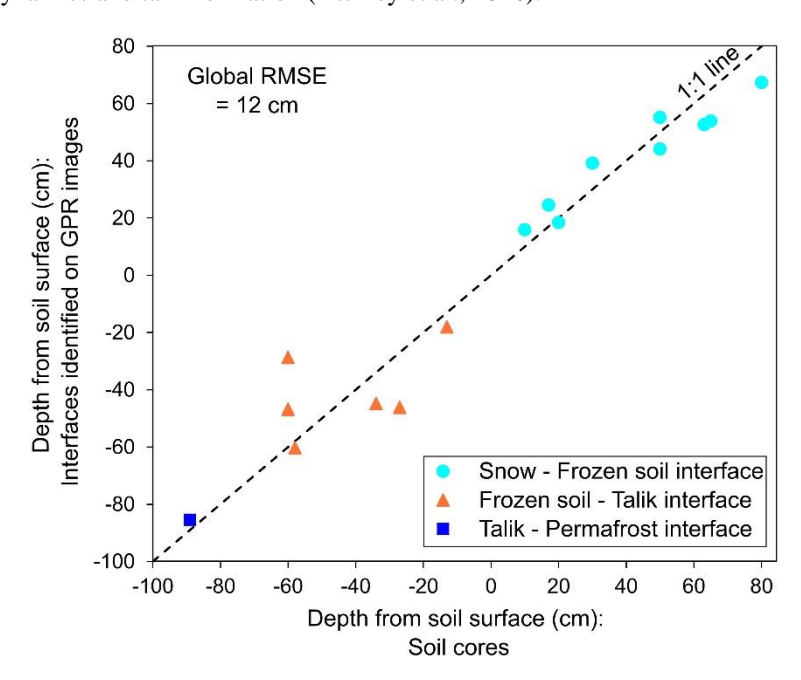


Figure 9: Comparison of the depths of the interfaces of interest (snow - frozen soil - talik, talik - permafrost) from the soil cores with those derived from the GPR interpretation.



455

460

465

470

475

480



450 **4.2 Taliks location and implications**

4.2.1 Taliks location and extent

The taliks detected in this study are suprapermafrost taliks, which form when the active layer fails to completely refreeze during winter (Devoie et al., 2019; Schuur et al., 2008). They were detected along a part of the transect and within all grids (covering 50 to 90 % of each grid area), indicating a widespread occurrence across the study site, even under the coldest annual soil temperatures. Given the warming of the permafrost in this area (Osterkamp et al., 2009), it is probable that taliks will expand over time. This is probably caused by rising Arctic temperatures (O'Neill et al., 2020).

Taliks were present preferentially in zones of localized subsidence and along water tracks. Regarding the depth of the tops of these taliks, their means ranged from 50 to 56 cm in the transect and upslope areas, whereas they were shallower in the middle and downslope zones (means between 33 and 45 cm, Table 2). In the middle and downslope areas, taliks were shallower than 45 cm in the water track paths. Taliks occurrence at shallower depths downslope and within water tracks relative to adjacent areas suggests more advanced permafrost degradation in these locations. Where quantifiable, talik thickness increased along the degradation sequence (mean of 26 cm in Grid 1, 33 cm in Grid 2, and 38 cm in Grid 5). Taliks were also thicker in water tracks, consistent with the deeper permafrost table there (Del Vecchio and Evans, 2025).

The taliks from the transect and Grids 1 and 2, not located on distinct water tracks, are likely isolated (i.e., surrounded by frozen ground) and confined to areas with more advanced permafrost degradation (Fig. B. 1d, Fig. 6d). In Grid 3, taliks may connect to their downstream counterparts within the water track but remain disconnected laterally (Fig. B. 2d). A similar pattern was observed for Grids 4 and 5, though their lateral connectivity to adjacent soil appear larger (Fig. B. 3d, Fig. 7d). In Grids 6 and 7, taliks appear to be connected to the upslope and downslope water track, and laterally to a part of the surrounding soil (Fig. B. 4d, Fig. 8d). It remains difficult to draw conclusions about the connectivity between the taliks and the groundwater in the area, as it was not directly monitored. The site's hydrological connectivity with the river and the lake is expected during part of the year, and to persist longer in talik areas in early winter, but it may still cease at some point during winter. Yet, the presence of water in the soil core hole at Grid 7 in March 2024 suggests that hydrological connectivity may persist throughout the whole winter season at that location.

4.2.2 Links between talik depth and environmental factors

Several factors influence talik formation such as snow cover, topography, soil moisture, vegetation and heat fluxes (Wang and Niu, 2024). First, snow acts as an insulator (Woo, 2012) preventing the ground from cooling, and triggering the appearance of deeper active layers and talik development (Atchley et al., 2016; Devoie et al., 2019; Jafarov et al., 2018; Johansson et al., 2013; O'Neill and Burn, 2017; Park et al., 2013). This was clearly observed in our study, where areas with thicker snow cover systematically corresponded to shallower taliks (overall Pearson correlation between snow thickness and



485

490

495

500

505



top of talik depth of -0.65, p-value < 0.001, Table C. 1). Second, topography plays a role in talik formation. This is particularly true for thermokarst landscapes, where the thawing of ice-rich permafrost causes surface subsidence (e.g., Kokelj and Jorgenson, 2013). In these depressions, the active layer thickens, and the permafrost is deeper (Johansson et al., 2013; Jones et al., 2016), which in turn promotes talik development (e.g., Sjöberg et al., 2015). In this study, taliks were more frequent in subsided areas upslope and were consistently shallower in surface depressions across all grids (overall Pearson correlation between top of talik depth and TPI of 0.53, p-value < 0.001, Table C. 1). Third, soil moisture can influence talik formation by increasing thermal conductivity (Devoie et al., 2019). In this study, shallower and thicker taliks were found in the middle and downslope areas (Table 2), where the talik soil was more humid. However, it is worth noting that water's high thermal capacity may also buffer temperature fluctuations.

All these talik formation factors are interdependent (Devoie et al., 2019) and reinforce one another through positive feedbacks. For instance, topographic depressions enhance snow accumulation (Devoie et al., 2019; Raudina et al., 2025; Woo, 2012) and increase soil moisture (Connon et al., 2018; Johansson et al., 2013). In turn, higher snow accumulation also contributes to higher soil moisture (Park et al., 2013; Woo, 2012; Zhang et al., 2005). Both thicker snow and higher soil moisture promote talik formation (Park et al., 2013). Finally, the presence of taliks contributes to surface subsidence (Devoie et al., 2019; Johansson et al., 2013). Water tracks represent a particular example of these interactions and feedbacks, as they are zones of higher soil moisture, thicker snow, and sometimes topographic depressions. This clearly identified water tracks as hotspots for talik formation and expansion.

4.2.3 Consequences of taliks presence along water tracks

Taliks' presence increases hydrological connectivity, particularly through lateral taliks that create preferential pathways for groundwater flow (Connon et al., 2018; O'Neill et al., 2020). This increases winter groundwater discharge (Lamontagne-Hallé et al., 2018) and strengthens the connection between hillslopes and rivers at this season (Tananaev et al., 2021). At this study site, groundwater fluxes likely occur within lateral taliks, although they are difficult to monitor and depend seasonally on the water availability (Kurylyk and Walvoord, 2021). These flows are expected to be more important in water tracks (Evans et al., 2020). This may allow the transport of organic carbon in winter and the delivery to inland waters (Walvoord et al., 2019). These enhanced water flows are also enabling heat transfer, which creates a positive feedback with talik expansion (Walvoord and Kurylyk, 2016).

4.3 Method strengths, limitations, and potential improvements

The use of GPR to detect talks provides valuable information about subsurface features that are not visible at the surface. Compared to probing with a metal rod, GPR is more accurate and versatile (Wang and Niu, 2024), and it is faster than core drilling (O'Neill et al., 2020). It is also particularly well suited for sensitive environments, as it minimizes disturbance. Thus, GPR provides high-resolution spatial data (dm-scale in this study) with relatively low effort. This could guide the placement





of soil cores and support the spatialization of their analysis. This study demonstrated the strong potential of GPR to deliver reliable information on talik distribution and extent. The use of three-dimensional data was especially valuable for characterizing the spatial continuity and connectivity of taliks and should be more widely adopted. Finally, future studies should pay particular attention to key landscape features such as water tracks, which may have disproportionate effects on talik formation and expansion.

520 This study faced several limitations, notably a lack of quantitative precision in identifying talik tops and the quasi-inability to detect talik bottoms. Talik identification was often less reliable outside water tracks due to lower contrast in GPR reflections. Then, the depth of detected talks depended on subjective interpretation and on estimated ε_r values. Additionally, the number of soil cores available for validation was limited. Several improvements could address these limitations. First, for better interpretation of GPR data, more soil cores should be collected, and multiple expert opinions could be compared. Using a 525 lower-frequency antenna (< 200 MHz) would enable the imaging of talik bottoms (Stevens and Moorman, 2008). Multichannel GPR could also increase precision and provide insights into soil moisture (Kneisel et al., 2008; Sudakova et al., 2021; Westermann et al., 2010). Other geophysical techniques could also be used to provide complementary information and provide more confidence in the interpretations (Sjöberg et al., 2015). Electrical resistivity tomography (ERT) is particularly recommended, as it provides information on subsurface material properties (Kneisel et al., 2008) and has proven useful for 530 talik detection (Sjöberg et al., 2015; You et al., 2017). Other complementary geophysical methods include electromagnetic induction, seismic methods, and nuclear magnetic resonance (Hauck et al., 2004; Kneisel et al., 2008; O'Neill et al., 2020). Finally, future work could extend the study to areas adjacent to water tracks and incorporate time-lapse measurements to investigate talik extent and evolution.

5 Conclusions

540

Taliks presence affects Arctic hydrology and carbon dynamics and represents an important threshold in permafrost degradation. Yet, taliks' distribution remains poorly studied. This study aimed to characterize the spatial distribution of suprapermafrost taliks using GPR in a discontinuous permafrost zone, with a specific focus on water tracks, through three-dimensional GPR grids. Below, we present the key conclusions corresponding to our three objectives.

(1) Ground-penetrating radar proved to be a reliable and efficient method for detecting taliks in three dimensions during winter in permafrost environments. Taliks were primarily located in water tracks and locally subsided zones. They were shallower (< 40 cm deep) and thicker (> 70 cm) in more degraded areas, especially downslope along water tracks. Upslope taliks appeared isolated, whereas downslope ones were laterally continuous, expanding along the water track and possibly to a part of the surrounding soil. This study also revealed significant correlations between talik depth and subsided topography (0.53), and between talik depth and snow accumulation (-0.65).





- 545 (2) Ground-penetrating radar successfully detected talik tops (RMSE = 17 cm) due to the electromagnetic contrast with the overlying frozen active layer. However, talik bottoms were not easily captured because of limited signal penetration depth.
 - (3) Water tracks were clearly identified as hotspots for talik formation and expansion, making them key features to study. This has important consequences regarding winter unfrozen soil connectivity, as well as for water and carbon fluxes.
- Future research could combine GPR with complementary geophysical techniques to improve talik characterization beneath water tracks aiming at precise volume estimations. Combining taliks volume determination with taliks groundwater flow in cold seasons would also provide important information. A monitoring across several years would also help to understand taliks evolution and persistence.





555 Appendix A: Dimensions of the GPR grids

Table A. 1: Positions along the slope and dimensions of the seven grids surveyed with GPR to produce three-dimensional data (width, length, area and line spacing).

	Position along the slope	Width (m)	Length (m)	Area (m ²)	Line spacing (m)
Grid 1	Upslope	26	31	825	1.5
Grid 2	Upslope	22	21	475	1.5
Grid 3	Upslope	22	22	515	2
Grid 4	Middle slope	16	25	415	1
Grid 5	Middle slope	13	25	350	1
Grid 6	Middle slope	28	52	1515	1
Grid 7	Downslope	20	31	630	1





560 Appendix B: Results of the GPR measurements for the remaining grids

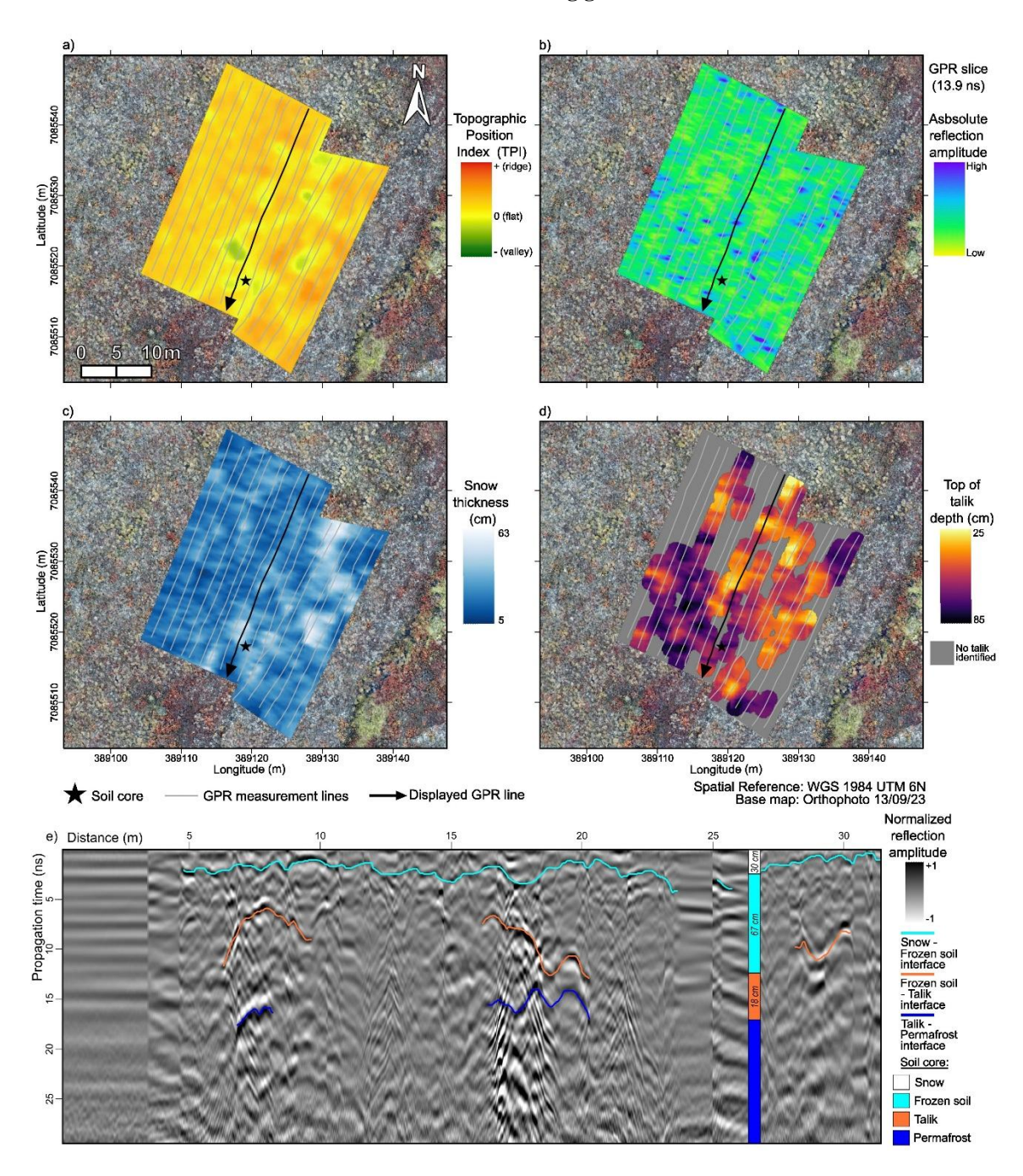


Figure B. 1: Results of the GPR measurements for Grid 1 (upslope). a) Topographic position index showing areas of subsidence. b) GPR horizontal slice at 13.9 ns two-way travel time, highlighting zones of strong reflections. c) Snow thickness derived from the GPR data. d) Depth of the top of the talik as interpreted from the GPR images. The grey area indicates locations where no talik was present or where it could not be identified with sufficient certainty. e) Vertical GPR slice at the soil core location, with visible interfaces of interest.





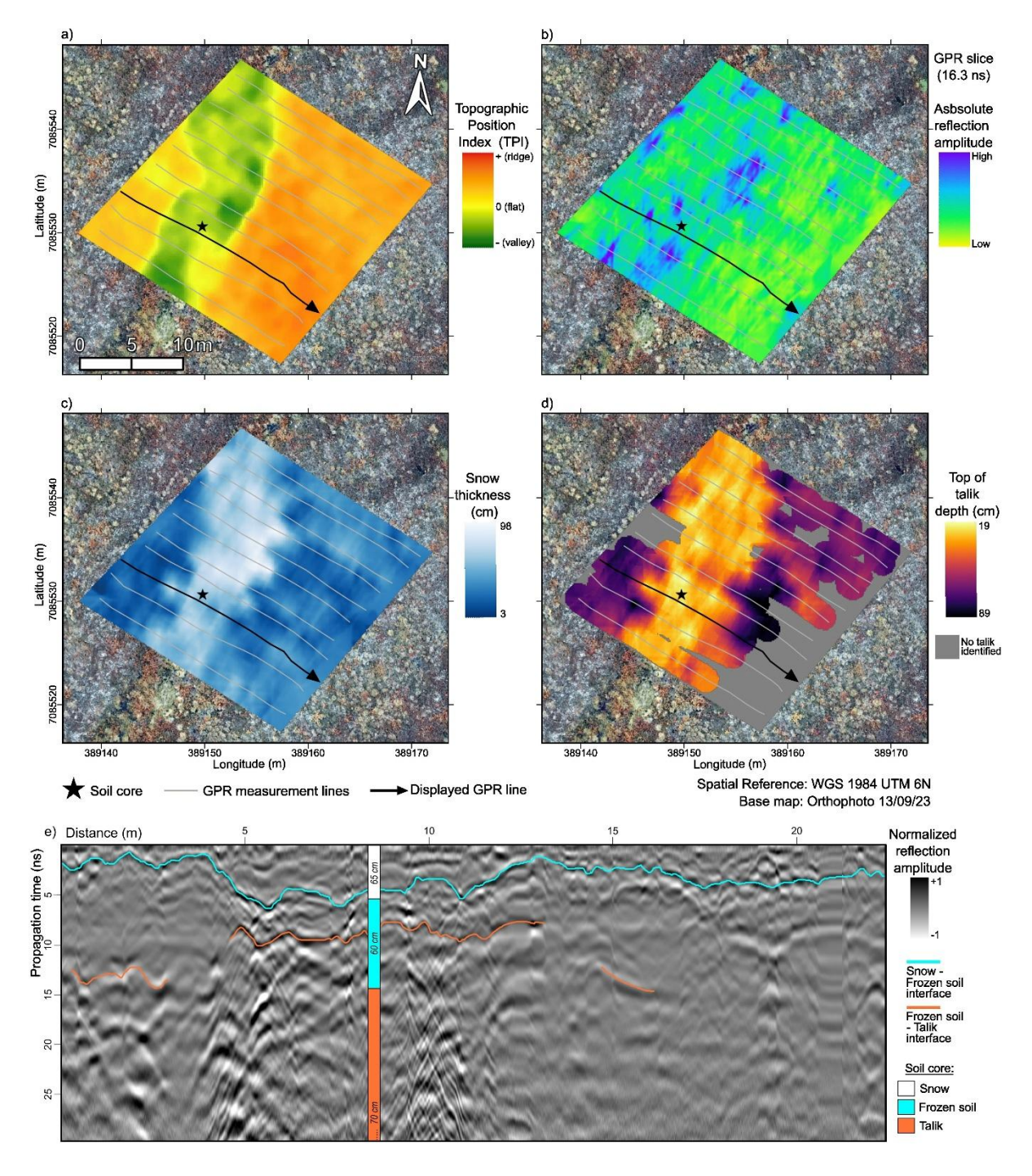


Figure B. 2: Results of the GPR measurements for Grid 3 (upslope). a) Topographic position index showing areas of subsidence. b) GPR horizontal slice at 16.3 ns two-way travel time, highlighting zones of strong reflections. c) Snow thickness derived from the GPR data. d) Depth of the top of the talik as interpreted from the GPR images. The grey area indicates locations where no talik was present or where it could not be identified with sufficient certainty. e) Vertical GPR slice at the soil core location, with visible interfaces of interest.





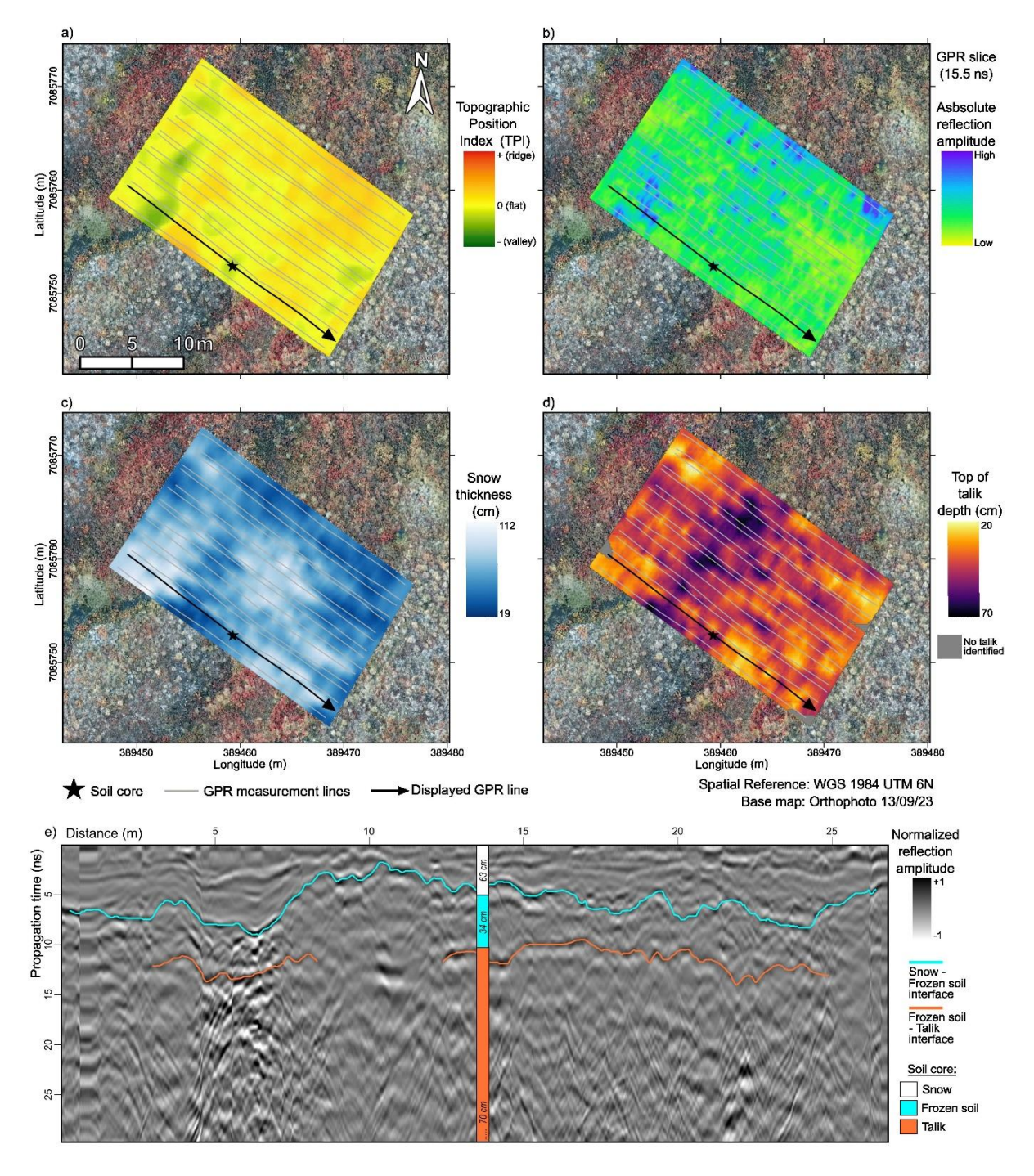


Figure B. 3: Results of the GPR measurements for Grid 4 (middle slope). a) Topographic position index showing areas of subsidence. b) GPR horizontal slice at 15.5 ns two-way travel time, highlighting zones of strong reflections. c) Snow thickness derived from the GPR data. d) Depth of the top of the talik as interpreted from the GPR images. The grey area indicates locations where no talik was present or where it could not be identified with sufficient certainty. e) Vertical GPR slice at the soil core location, with visible interfaces of interest.





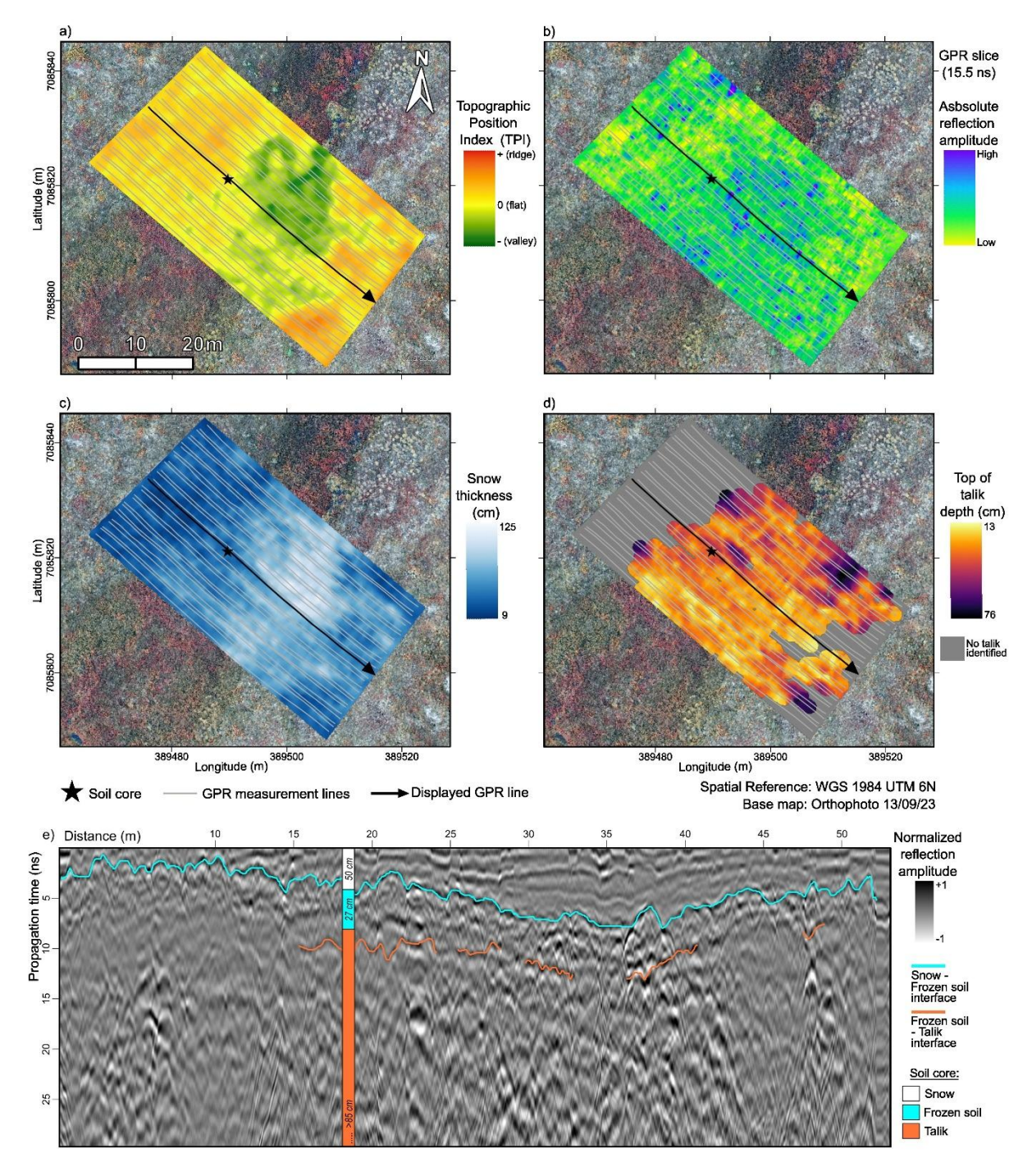


Figure B. 4: Results of the GPR measurements for Grid 6 (middle slope). a) Topographic position index showing areas of subsidence. b) GPR horizontal slice at 15.5 ns two-way travel time, highlighting zones of strong reflections. c) Snow thickness derived from the GPR data. d) Depth of the top of the talik as interpreted from the GPR images. The grey area indicates locations where no talik was present or where it could not be identified with sufficient certainty. e) Vertical GPR slice at the soil core location, with visible interfaces of interest.





Appendix C: Correlations between snow thickness, surface subsidence, and talik thickness across the grids

Table C. 1: Pearson correlations between snow thickness and top of talik depth and between TPI and top of talik depth across the seven grids. Due to the large number of observation points per grid (>29500), all the correlations are statistically significant (p-value < 0.001).

	Grid 1	Grid 2	Grid 3	Grid 4	Grid 5	Grid 6	Grid 7	All Grids
Correlation between snow	-0.36	-0.71	-0.77	-0.37	-0.63	-0.33	-0.70	-0.65
thickness and top of talik								
depth								
Correlation between TPI and	0.06	0.20	0.72	0.19	0.56	0.29	0.58	0.53
top of talik depth								

https://doi.org/10.5194/egusphere-2025-4667 Preprint. Discussion started: 27 October 2025

© Author(s) 2025. CC BY 4.0 License.



EGUsphere Preprint repository

Data availability

All GPR data will be made available publicly on Zenodo upon publication of the manuscript. These can be previewed by the

reviewers using the link provided in the submission procedure.

595 Author contribution

MH, SO, and SL conceptualized the study. ES and SL provided resources. MH, SO, MV, PR, and GD carried out the investigation. MH developed the methodology, performed the formal analysis, and created the visualizations. SO, FJ, VV, KVO, and SL acquired funding. MH prepared the manuscript under the supervision of SO and SL, and all authors

contributed to its review.

600 Competing interests

The authors declare that they have no conflict of interest.

Acknowledgments

605

The authors thank Justin Ledman for his logistical support on the field and help with the soil core sampling auger. We thank Sébastien François for his logistical support in preparing the field mission. Cécile Osy assisted with the Teros12 sensor installation. Bruno Delille provided advice and field equipment for winter conditions, and IMAQA provided training for fieldwork in extreme conditions. Sophie Opfergelt, Kristof Van Oost, and Sébastien Lambot are supported by the *Fonds de*

la Recherche Scientifique (FNRS). ChatGPT was used in order to improve the language of the manuscript.

Financial support

This work is part of the *Action de Recherche Concertée*, LandSense project (n° 21/26-119), funded by the *Fédération*610 *Wallonie-Bruxelles*. A *Crédit de Recherche* accorded by the *Fonds de la Recherche Scientifique* to Sébastien Lambot, with

contract number J.0122.24, funded the field mission.





References

- Arcone, S. A. and Delaney, A. J.: Dielectric properties of thawed active layers overlying permafrost using radar at VHF, Radio Sci., 17, 618–626, https://doi.org/10.1029/RS017i003p00618, 1982.
 - Arcone, S. A., Lawson, D. E., Delaney, J., Strasser, J. C., and Strasser, J. D.: Ground-penetrating radar reflection profiling of groundwater and bedrock in an area of discontinuous permafrost, Geophysics, 63, 1998a.
 - Arcone, S. A., Chacho, E. F., and Delaney, A. J.: Seasonal structure of taliks beneath arctic streams determined with ground-penetrating radar, in: PERMAFROST Seventh International Conference (Proceedings), Canada, 1998b.
- Ardekani, M. R., Druyts, P., Lambot, S., De Coster, A., and Neyt, X.: Recovering the structure of a layered soil, including layer thickness and dielectric permittivity, using the interfaces and objects backscatter detected in GPR B-scans, in: Proceedings of the 15th International Conference on Ground Penetrating Radar, Brussels, 397–400, https://doi.org/10.1109/ICGPR.2014.6970454, 2014.
- Arndt, K. A., Hashemi, J., Natali, S. M., Schiferl, L. D., and Virkkala, A.-M.: Recent Advances and Challenges in Monitoring and Modeling Non-Growing Season Carbon Dioxide Fluxes from the Arctic Boreal Zone, Curr. Clim. Change Rep., 9, 27–40, https://doi.org/10.1007/s40641-023-00190-4, 2023.
 - Atchley, A. L., Coon, E. T., Painter, S. L., Harp, D. R., and Wilson, C. J.: Influences and interactions of inundation, peat, and snow on active layer thickness, Geophys. Res. Lett., 43, 5116–5123, https://doi.org/10.1002/2016GL068550, 2016.
- Biskaborn, B. K., Smith, S. L., Noetzli, J., Matthes, H., Vieira, G., Streletskiy, D. A., Schoeneich, P., Romanovsky, V. E., Lewkowicz, A. G., Abramov, A., Allard, M., Boike, J., Cable, W. L., Christiansen, H. H., Delaloye, R., Diekmann, B., Drozdov, D., Etzelmüller, B., Grosse, G., Guglielmin, M., Ingeman-Nielsen, T., Isaksen, K., Ishikawa, M., Johansson, M., Johannsson, H., Joo, A., Kaverin, D., Kholodov, A., Konstantinov, P., Kröger, T., Lambiel, C., Lanckman, J.-P., Luo, D., Malkova, G., Meiklejohn, I., Moskalenko, N., Oliva, M., Phillips, M., Ramos, M., Sannel, A. B. K., Sergeev, D., Seybold, C., Skryabin, P., Vasiliev, A., Wu, Q., Yoshikawa, K., Zheleznyak, M., and Lantuit, H.: Permafrost is warming at a global scale, Nat. Commun., 10, 264, https://doi.org/10.1038/s41467-018-08240-4, 2019.
 - Boike, J., Roth, K., and Overduin, P. P.: Thermal and hydrologic dynamics of the active layer at a continuous permafrost site (Taymyr Peninsula, Siberia), Water Resour. Res., 34, 355–363, https://doi.org/10.1029/97WR03498, 1998.
- Brosten, T. R., Bradford, J. H., McNamara, J. P., Gooseff, M. N., Zarnetske, J. P., Bowden, W. B., and Johnston, M. E.: Estimating 3D variation in active-layer thickness beneath arctic streams using ground-penetrating radar, J. Hydrol., 373, 479–486, https://doi.org/10.1016/j.jhydrol.2009.05.011, 2009.
- Burn, C. R., Bartsch, A., Chakraborty, E., Das, S., Frauenfelder, R., Gärtner-Roer, I., Gisnås, K. G., Herring, T., Jones, B. M., Kokelj, S. V., Langer, M., Lathrop, E., Murton, J. B., Nielsen, D. M., Niu, F., Olson, C., O'Neill, H. B., Opfergelt, S., Overduin, P. P., Schaefer, K., Schuur, E. A. G., Skierszkan, E., Smith, S. L., Stuenzi, S. M., Tank, S. E., van der Sluijs, J., Vieira, G., Westermann, S., Wolfe, S. A., and Yarmak, E.: Developments in Permafrost Science and Engineering in Response to Climate Warming in Circumpolar and High Mountain Regions, 2019–2024, Permafrost Periglacial Processes, 2261, https://doi.org/10.1002/ppp.2261, 2024.
 - Connon, R., Devoie, É., Hayashi, M., Veness, T., and Quinton, W.: The Influence of Shallow Taliks on Permafrost Thaw and Active Layer Dynamics in Subarctic Canada, JGR Earth Surface, 123, 281–297, https://doi.org/10.1002/2017JF004469, 2018.
- Daniels, D. J. (Ed.): Signal processing, in: Ground penetrating radar, vol. 1, London, United Kingdom, 2004.





- Davis, J. L., Scott, W. J., Morey, R. M., and Annan, A. P.: Impulse radar experiments on permafrost near Tuktoyaktuk, Northwest Territories, Can. J. Earth Sci., 13, 1584–1590, https://doi.org/10.1139/e76-165, 1976.
- Del Vecchio, J. and Evans, S. G.: Climate and Hydrogeological Controls on Water Tracks in Permafrost Landscapes, Rev. Geophys., 63, e2024RG000854, https://doi.org/10.1029/2024RG000854, 2025.
- Devoie, É., Connon, R. F., Beddoe, R., Goordial, J., Quinton, W. L., and Craig, J. R.: Disconnected active layers and unfrozen permafrost: A discussion of permafrost-related terms and definitions, Sci. Total Environ., 912, 169017, https://doi.org/10.1016/j.scitotenv.2023.169017, 2024.
 - Devoie, É. G., Craig, J. R., Connon, R. F., and Quinton, W. L.: Taliks: A Tipping Point in Discontinuous Permafrost Degradation in Peatlands, Water Resour. Res., 55, 9838–9857, https://doi.org/10.1029/2018WR024488, 2019.
- Di Paolo, F., Cosciotti, B., Lauro, S. E., Mattei, E., and Pettinelli, E.: Dry snow permittivity evaluation from density: A critical review, in: Proceedings 17th International Conference on Ground Penetrating Radar, Rapperswil, Switzerland, 1–5, https://doi.org/10.1109/ICGPR.2018.8441610, 2018.
 - Doolittle, J. A.: Using Ground-penetrating Radar to Increase the Quality and Efficiency of Soil Surveys, in: Soil Surveys Techniques, Soil Science Society of America, 11–32, 1987.
- 665 Evans, S.: Dielectric Properties of Ice and Snow-a Review, J. Glaciol., 5, 773–792, https://doi.org/10.3189/S0022143000018840, 1965.
 - Evans, S. G., Godsey, S. E., Rushlow, C. R., and Voss, C.: Water Tracks Enhance Water Flow Above Permafrost in Upland Arctic Alaska Hillslopes, JGR Earth Surface, 125, e2019JF005256, https://doi.org/10.1029/2019JF005256, 2020.
- Farquharson, L. M., Romanovsky, V. E., Kholodov, A., and Nicolsky, D.: Sub-aerial talik formation observed across the discontinuous permafrost zone of Alaska, Nat. Geosci., 15, 475–481, https://doi.org/10.1038/s41561-022-00952-z, 2022.
 - Hallikainen, M., Ulaby, F., and Abdelrazik, M.: Dielectric properties of snow in the 3 to 37 GHz range, IEEE Trans. Antennas Propag., 34, 1329–1340, https://doi.org/10.1109/TAP.1986.1143757, 1986.
- Hauck, C., Isaksen, K., Vonder Mühll, D., and Sollid, J. L.: Geophysical surveys designed to delineate the altitudinal limit of mountain permafrost: an example from Jotunheimen, Norway, Permafrost Periglacial Processes, 15, 191–205, https://doi.org/10.1002/ppp.493, 2004.
 - He, H. and Dyck, M.: Application of Multiphase Dielectric Mixing Models for Understanding the Effective Dielectric Permittivity of Frozen Soils, Vadose Zone J., 12, 1–22, https://doi.org/10.2136/vzj2012.0060, 2013.
- Henrion, M., Li, Y., Koganti, T., Bechtold, M., Jonard, F., Opfergelt, S., Vanacker, V., Van Oost, K., and Lambot, S.: Mapping and monitoring peatlands in the Belgian Hautes Fagnes: Insights from Ground-penetrating radar and Electromagnetic induction characterization, Geoderma Regional, 37, https://doi.org/10.1016/j.geodrs.2024.e00795, 2024.
 - Hicks Pries, C. E., Schuur, E. A. G., and Crummer, K. G.: Holocene Carbon Stocks and Carbon Accumulation Rates Altered in Soils Undergoing Permafrost Thaw, Ecosystems, 15, 162–173, https://doi.org/10.1007/s10021-011-9500-4, 2012.
- Hinkel, K. M., Doolittle, J. A., Bockheim, J. G., Nelson, F. E., Paetzold, R., Kimble, J. M., and Travis, R.: Detection of subsurface permafrost features with ground-penetrating radar, Barrow, Alaska, Permafrost Periglacial Processes, 12, 179–190, https://doi.org/10.1002/ppp.369, 2001.





- Jafarov, E. E., Coon, E. T., Harp, D. R., Wilson, C. J., Painter, S. L., Atchley, A. L., and Romanovsky, V. E.: Modeling the role of preferential snow accumulation in through talik development and hillslope groundwater flow in a transitional permafrost landscape, Environ. Res. Lett., 13, 105006, https://doi.org/10.1088/1748-9326/aadd30, 2018.
- Johansson, M., Callaghan, T. V., Bosiö, J., Åkerman, H. J., Jackowicz-Korczynski, M., and Christensen, T. R.: Rapid responses of permafrost and vegetation to experimentally increased snow cover in sub-arctic Sweden, Environ. Res. Lett., 8, 035025, https://doi.org/10.1088/1748-9326/8/3/035025, 2013.
 - Jones, B. M., Baughman, C. A., Romanovsky, V. E., Parsekian, A. D., Babcock, E. L., Stephani, E., Jones, M. C., Grosse, G., and Berg, E. E.: Presence of rapidly degrading permafrost plateaus in south-central Alaska, The Cryosphere, 10, 2673–2692, https://doi.org/10.5194/tc-10-2673-2016, 2016.
- Kneisel, C., Hauck, C., Fortier, R., and Moorman, B.: Advances in geophysical methods for permafrost investigations, Permafrost Periglacial Processes, 19, 157–178, https://doi.org/10.1002/ppp.616, 2008.
 - Kokelj, S. V. and Jorgenson, M. T.: Advances in Thermokarst Research, Permafrost Periglacial Processes, 24, 108–119, https://doi.org/10.1002/ppp.1779, 2013.
- Koven, C. D., Ringeval, B., Friedlingstein, P., Ciais, P., Cadule, P., Khvorostyanov, D., Krinner, G., and Tarnocai, C.: 700 Permafrost carbon-climate feedbacks accelerate global warming, PNAS, 108, 14769–14774, https://doi.org/10.1073/pnas.1103910108, 2011.
 - Kurylyk, B. L. and Walvoord, M. A.: Permafrost Hydrogeology, in: Arctic Hydrology, Permafrost and Ecosystems, edited by: Yang, D. and Kane, D. L., Springer International Publishing, Cham, https://doi.org/10.1007/978-3-030-50930-9, 2021.
- Lamontagne-Hallé, P., McKenzie, J. M., Kurylyk, B. L., and Zipper, S. C.: Changing groundwater discharge dynamics in permafrost regions, Environ. Res. Lett., 13, 084017, https://doi.org/10.1088/1748-9326/aad404, 2018.
 - Lyu, Z., Sommers, P., Schmidt, S. K., Magnani, M., Cimpoiasu, M., Kuras, O., Zhuang, Q., Oh, Y., De La Fuente, M., Cramm, M., and Bradley, J. A.: Seasonal dynamics of Arctic soils: Capturing year-round processes in measurements and soil biogeochemical models, Earth Sci. Rev., 254, 104820, https://doi.org/10.1016/j.earscirev.2024.104820, 2024.
- Mauclet, E., Agnan, Y., Hirst, C., Monhonval, A., Pereira, B., Vandeuren, A., Villani, M., Ledman, J., Taylor, M., Jasinski,
 B. L., Schuur, E. A. G., and Opfergelt, S.: Changing sub-Arctic tundra vegetation upon permafrost degradation: impact on foliar mineral element cycling, Biogeosciences, 19, 2333–2351, https://doi.org/10.5194/bg-19-2333-2022, 2022.
 - Monhonval, A., Mauclet, E., Hirst, C., Bemelmans, N., Eekman, E., Schuur, E. A. G., and Opfergelt, S.: Mineral organic carbon interactions in dry versus wet tundra soils, Geoderma, 436, 116552, https://doi.org/10.1016/j.geoderma.2023.116552, 2023.
- Moorman, B. J., Robinson, S. D., and Burgess, M. M.: Imaging periglacial conditions with ground-penetrating radar, Permafrost & Periglacial, 14, 319–329, https://doi.org/10.1002/ppp.463, 2003.
 - Munroe, J. S., Doolittle, J. A., Kanevskiy, M. Z., Hinkel, K. M., Nelson, F. E., Jones, B. M., Shur, Y., and Kimble, J. M.: Application of ground-penetrating radar imagery for three-dimensional visualisation of near-surface structures in ice-rich permafrost, Barrow, Alaska, Permafrost Periglacial Processes, 18, 309–321, https://doi.org/10.1002/ppp.594, 2007.
- Natali, S. M., Watts, J. D., Rogers, B. M., Potter, S., Ludwig, S. M., Selbmann, A.-K., Sullivan, P. F., Abbott, B. W., Arndt, K. A., Birch, L., Björkman, M. P., Bloom, A. A., Celis, G., Christensen, T. R., Christiansen, C. T., Commane, R., Cooper, E. J., Crill, P., Czimczik, C., Davydov, S., Du, J., Egan, J. E., Elberling, B., Euskirchen, E. S., Friborg, T., Genet, H., Göckede,





- M., Goodrich, J. P., Grogan, P., Helbig, M., Jafarov, E. E., Jastrow, J. D., Kalhori, A. A. M., Kim, Y., Kimball, J. S., Kutzbach, L., Lara, M. J., Larsen, K. S., Lee, B.-Y., Liu, Z., Loranty, M. M., Lund, M., Lupascu, M., Madani, N., Malhotra,
- A., Matamala, R., McFarland, J., McGuire, A. D., Michelsen, A., Minions, C., Oechel, W. C., Olefeldt, D., Parmentier, F.-J. W., Pirk, N., Poulter, B., Quinton, W., Rezanezhad, F., Risk, D., Sachs, T., Schaefer, K., Schmidt, N. M., Schuur, E. A. G., Semenchuk, P. R., Shaver, G., Sonnentag, O., Starr, G., Treat, C. C., Waldrop, M. P., Wang, Y., Welker, J., Wille, C., Xu, X., Zhang, Z., Zhuang, Q., and Zona, D.: Large loss of CO2 in winter observed across the northern permafrost region, Nat. Clim. Chang., 9, 852–857, https://doi.org/10.1038/s41558-019-0592-8, 2019.
- Neal, A.: Ground-penetrating radar and its use in sedimentology: principles, problems and progress, Earth-Science Reviews, 66, 261–330, https://doi.org/10.1016/j.earscirev.2004.01.004, 2004.
 - Olsson, P. Q., Sturm, M., Racine, C. H., Romanovsky, V., and Liston, G. E.: Five Stages of the Alaskan Arctic Cold Season with Ecosystem Implications, Arctic, Antarctic, and Alpine Research, 35, 74–81, https://doi.org/10.1657/1523-0430(2003)035[0074:FSOTAA]2.0.CO;2, 2003.
- O'Neill, H. B. and Burn, C. R.: Talik Formation at a Snow Fence in Continuous Permafrost, Western Arctic Canada, Permafrost Periglacial Processes, 28, 558–565, https://doi.org/10.1002/ppp.1905, 2017.
 - O'Neill, H. B., Roy-Leveillee, P., Lebedeva, L., and Ling, F.: Recent advances (2010–2019) in the study of taliks, Permafrost Periglacial Processes, 31, 346–357, https://doi.org/10.1002/ppp.2050, 2020.
- Ortet, J., Mialon, A., Royer, A., Schwank, M., Holmberg, M., Rautiainen, K., Bircher-Adrot, S., Colliander, A., Kerr, Y., and Roy, A.: Retrieving frozen ground surface temperature under the snowpack in Arctic permafrost area from SMOS observations, The Cryosphere, 19, 3571–3598, https://doi.org/10.5194/tc-19-3571-2025, 2025.
 - Osterkamp, T. E., Jorgenson, M. T., Schuur, E. A. G., Shur, Y. L., Kanevskiy, M. Z., Vogel, J. G., and Tumskoy, V. E.: Physical and ecological changes associated with warming permafrost and thermokarst in Interior Alaska, Permafrost Periglacial Processes, 20, 235–256, https://doi.org/10.1002/ppp.656, 2009.
- Pan, X., You, Y., Roth, K., Guo, L., Wang, X., and Yu, Q.: Mapping Permafrost Features that Influence the Hydrological Processes of a Thermokarst Lake on the Qinghai-Tibet Plateau, China, Permafrost Periglacial Processes, 25, 60–68, https://doi.org/10.1002/ppp.1797, 2014.
- Parazoo, N. C., Koven, C. D., Lawrence, D. M., Romanovsky, V., and Miller, C. E.: Detecting the permafrost carbon feedback: talik formation and increased cold-season respiration as precursors to sink-to-source transitions, The Cryosphere, 12, 123–144, https://doi.org/10.5194/tc-12-123-2018, 2018.
 - Park, H., Walsh, J., Fedorov, A. N., Sherstiukov, A. B., Iijima, Y., and Ohata, T.: The influence of climate and hydrological variables on opposite anomaly in active-layer thickness between Eurasian and North American watersheds, The Cryosphere, 7, 631–645, https://doi.org/10.5194/tc-7-631-2013, 2013.
- Pepin, S., Plamondon, A., and Stein, J.: Peat water content measurement using time domain reflectometry, Can. J. For. Res., 22, 534–540, 1992.
 - Permafrost Subcommittee (Ed.): Glossary of permafrost and related ground-ice terms, National Research Council Canada., Ottawa, Canada, 156 pp., 1988.
- Plaza, C., Pegoraro, E., Bracho, R., Celis, G., Crummer, K. G., Hutchings, J. A., Hicks Pries, C. E., Mauritz, M., Natali, S. M., Salmon, V. G., Schädel, C., Webb, E. E., and Schuur, E. A. G.: Direct observation of permafrost degradation and rapid soil carbon loss in tundra, Nat. Geosci., 12, 627–631, https://doi.org/10.1038/s41561-019-0387-6, 2019.





- Popov, S. V., Kashkevich, M. P., Romanova, N. E., Malysheva, A. M., and Lebedeva, L. S.: Identification of subaerial taliks by geophysical methods in the middle part of the Lena River basin, Central Yakutia, J. Min. Inst., 2025.
- Raudina, T. V., Loiko, S. V., Istigechev, G. I., Kulizhskiy, S. P., Orgogozo, L., and Pokrovsky, O. S.: Contrasting soil temperature regimes in peatlands of the discontinuous permafrost zone (Western Siberia), Geoderma, 457, 117294, https://doi.org/10.1016/j.geoderma.2025.117294, 2025.
 - Rey, D. M., Walvoord, M. A., Minsley, B. J., Ebel, B. A., Voss, C. I., and Singha, K.: Wildfire-Initiated Talik Development Exceeds Current Thaw Projections: Observations and Models From Alaska's Continuous Permafrost Zone, Geophys. Res. Lett., 47, https://doi.org/10.1029/2020gl087565, 2020.
- Rodenhizer, H., Ledman, J., Mauritz, M., Natali, S. M., Pegoraro, E., Plaza, C., Romano, E., Schädel, C., Taylor, M., and Schuur, E.: Carbon Thaw Rate Doubles When Accounting for Subsidence in a Permafrost Warming Experiment, JGR Biogeosciences, 125, e2019JG005528, https://doi.org/10.1029/2019JG005528, 2020.
 - Rodenhizer, H., Belshe, F., Celis, G., Ledman, J., Goetz, S., Sankey, T., and Schuur, E. A. G.: Abrupt permafrost thaw accelerates carbon dioxide and methane release at a tussock tundra site, Arctic, Antarctic, and Alpine Research, 54, 443–464, 2022.
- Schuur, E. A. G., Crummer, K. G., Vogel, J. G., and Mack, M. C.: Plant Species Composition and Productivity following Permafrost Thaw and Thermokarst in Alaskan Tundra, Ecosystems, 10, 280–292, https://doi.org/10.1007/s10021-007-9024-0, 2007.
- Schuur, E. A. G., Bockheim, J., Canadell, J. G., Euskirchen, E., Field, C. B., Goryachkin, S. V., Hagemann, S., Kuhry, P., Lafleur, P. M., Lee, H., Mazhitova, G., Nelson, F. E., Rinke, A., Romanovsky, V. E., Shiklomanov, N., Tarnocai, C., Venevsky, S., Vogel, J. G., and Zimov, S. A.: Vulnerability of Permafrost Carbon to Climate Change: Implications for the Global Carbon Cycle, BioScience, 58, 701–714, https://doi.org/10.1641/B580807, 2008.
 - Schuur, E. A. G., Vogel, J. G., Crummer, K. G., Lee, H., Sickman, J. O., and Osterkamp, T. E.: The effect of permafrost thaw on old carbon release and net carbon exchange from tundra, Nature, 459, 556–559, https://doi.org/10.1038/nature08031, 2009.
- Schuur, E. A. G., McGuire, A. D., Schädel, C., Grosse, G., Harden, J. W., Hayes, D. J., Hugelius, G., Koven, C. D., Kuhry, P., Lawrence, D. M., Natali, S. M., Olefeldt, D., Romanovsky, V. E., Schaefer, K., Turetsky, M. R., Treat, C. C., and Vonk, J. E.: Climate change and the permafrost carbon feedback, Nature, 520, 171–179, https://doi.org/10.1038/nature14338, 2015.
- Schuur, E. A. G., Bracho, R., Celis, G., Belshe, E. F., Ebert, C., Ledman, J., Mauritz, M., Pegoraro, E. F., Plaza, C., Rodenhizer, H., Romanovsky, V., Schädel, C., Schirokauer, D., Taylor, M., Vogel, J. G., and Webb, E. E.: Tundra Underlain By Thawing Permafrost Persistently Emits Carbon to the Atmosphere Over 15 Years of Measurements, JGR Biogeosciences, 126, e2020JG006044, https://doi.org/10.1029/2020JG006044, 2021.
 - Sjöberg, Y., Marklund, P., Pettersson, R., and Lyon, S. W.: Geophysical mapping of palsa peatland permafrost, The Cryosphere, 9, 465–478, https://doi.org/10.5194/tc-9-465-2015, 2015.
- Stevens, C. W. and Moorman, B. J.: Detection of Frozen and Unfrozen Interfaces with Ground Penetrating Radar in the Nearshore Zone of the Mackenzie Delta, Canada, in: Proceedings Ninth International Conference on Permafrost, 2008.
 - Sudakova, M., Sadurtdinov, M., Skvortsov, A., Tsarev, A., Malkova, G., Molokitina, N., and Romanovsky, V.: Using Ground Penetrating Radar for Permafrost Monitoring from 2015–2017 at CALM Sites in the Pechora River Delta, Remote Sensing, 13, 3271, https://doi.org/10.3390/rs13163271, 2021.





- Tananaev, N., Isaev, V., Sergeev, D., Kotov, P., and Komarov, O.: Hydrological Connectivity in a Permafrost Tundra Landscape near Vorkuta, North-European Arctic Russia, Hydrology, 8, 106, https://doi.org/10.3390/hydrology8030106, 2021.
 - Topp, G. C. and Davis, J. L.: Measurement of Soil Water Content using Time-domain Reflectrometry (TDR): A Field Evaluation, Soil Sci. Soc. Am. J., 49, 19–24, https://doi.org/10.2136/sssaj1985.03615995004900010003x, 1985.
- Vogel, J., Schuur, E. A. G., Trucco, C., and Lee, H.: Response of CO2 exchange in a tussock tundra ecosystem to permafrost thaw and thermokarst development, JGR Biogeosciences, 114, 2008JG000901, https://doi.org/10.1029/2008JG000901, 2009
 - Walvoord, M. A. and Kurylyk, B. L.: Hydrologic Impacts of Thawing Permafrost—A Review, Vadose Zone J., 15, 1–20, https://doi.org/10.2136/vzj2016.01.0010, 2016.
- Walvoord, M. A., Voss, C. I., Ebel, B. A., and Minsley, B. J.: Development of perennial thaw zones in boreal hillslopes enhances potential mobilization of permafrost carbon, Environ. Res. Lett., 14, 015003, https://doi.org/10.1088/1748-9326/aaf0cc, 2019.
 - Wang, Y. and Niu, F.: Advancements in Talik Research and a Novel Approach to Treatment for Talik beneath Subgrade, J. Cold Reg. Eng., 38, 03124002, https://doi.org/10.1061/JCRGEI.CRENG-779, 2024.
- Watanabe, K. and Wake, T.: Measurement of unfrozen water content and relative permittivity of frozen unsaturated soil using NMR and TDR, Cold Reg. Sci.Technol., 59, 34–41, https://doi.org/10.1016/j.coldregions.2009.05.011, 2009.
 - Weiss, A.: Topographic Position and Landforms Analysis, in: ESRI user conference, San Diego, United States of America, 2001
 - Westermann, S., Wollschläger, U., and Boike, J.: Monitoring of active layer dynamics at a permafrost site on Svalbard using multi-channel ground-penetrating radar, The Cryosphere, 4, 475–487, https://doi.org/10.5194/tc-4-475-2010, 2010.
- 820 Woo, M.: Snow Cover, in: Permafrost Hydrology, Springer Berlin Heidelberg, Berlin, Heidelberg, https://doi.org/10.1007/978-3-642-23462-0, 2012.
 - Yoshikawa, K. and Hinzman, L. D.: Shrinking thermokarst ponds and groundwater dynamics in discontinuous permafrost near council, Alaska, Permafrost Periglacial Processes, 14, 151–160, https://doi.org/10.1002/ppp.451, 2003.
- You, Y., Yu, Q., Pan, X., Wang, X., and Guo, L.: Geophysical Imaging of Permafrost and Talik Configuration Beneath a Thermokarst Lake: Imaging Permafrost and Talik of a Thermokarst Lake, Permafrost Periglacial Processes, 28, 470–476, https://doi.org/10.1002/ppp.1938, 2017.
 - Zhang, T., Frauenfeld, O. W., Serreze, M. C., Etringer, A., Oelke, C., McCreight, J., Barry, R. G., Gilichinsky, D., Yang, D., Ye, H., Ling, F., and Chudinova, S.: Spatial and temporal variability in active layer thickness over the Russian Arctic drainage basin, JGR Atmospheres, 110, 2004JD005642, https://doi.org/10.1029/2004JD005642, 2005.